



ELSEVIER

Contents lists available at ScienceDirect

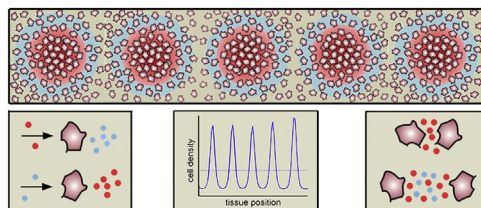
Journal of Theoretical Biology

journal homepage: www.elsevier.com/locate/jtbi

Modeling the morphodynamic galectin patterning network of the developing avian limb skeleton

T. Glimm^{a,*}, R. Bhat^b, S.A. Newman^c^a Department of Mathematics, Western Washington University, Bellingham, WA 98229, USA^b Life Sciences Division, Lawrence Berkeley National Laboratory, Berkeley, CA 94720, USA^c Department of Cell Biology & Anatomy, Basic Sciences Building, Valhalla, NY 10595, USA

GRAPHICAL ABSTRACT



ARTICLE INFO

Article history:

Received 16 July 2013

Received in revised form

27 November 2013

Accepted 2 December 2013

Available online 16 December 2013

Keywords:

Limb development

Chondrogenesis

Pattern formation

Nonlocal reaction–diffusion model

Partial integro-differential equations

ABSTRACT

We present a mathematical model for the morphogenesis and patterning of the mesenchymal condensations that serve as primordia of the avian limb skeleton. The model is based on the experimentally established dynamics of a multiscale regulatory network consisting of two glycan-binding proteins expressed early in limb development: CG (chicken galectin)-1A, CG-8 and their counterreceptors that determine the formation, size, number and spacing of the “protocondensations” that give rise to the condensations and subsequently the cartilaginous elements that serve as the templates of the bones. The model, a system of partial differential and integro-differential equations containing a flux term to represent local adhesion gradients, is simulated in a “full” and a “reduced” form to confirm that the system has pattern-forming capabilities and to explore the nature of the patterning instability. The full model recapitulates qualitatively and quantitatively the experimental results of network perturbation and leads to new predictions, which are verified by further experimentation. The reduced model is used to demonstrate that the patterning process is inherently morphodynamic, with cell motility being intrinsic to it. Furthermore, subtle relationships between cell movement and the positive and negative interactions between the morphogens produce regular patterns without the requirement for activators and inhibitors with widely separated diffusion coefficients. The described mechanism thus represents an extension of the category of activator–inhibitor processes capable of generating biological patterns with repetitive elements beyond the morphostatic mechanisms of the Turing/Gierer–Meinhardt type.

© 2013 Elsevier Ltd. All rights reserved.

1. Introduction

The organization of cells and tissues into specific arrangements or patterns during embryogenesis, and the inheritance of these

pattern-forming mechanisms, constitute important problems of both developmental and evolutionary biology (Müller et al., 2007). The patterning of the skeletal elements in vertebrate limbs is an experimental system within which these issues have received particular attention (Newman and Bhat, 2007).

The quasi-periodic arrangement of limb bones is well conserved across the tetrapods and consists of a progressive increase in element number along the proximal–distal axis (Saunders, 1948). Each skeletal element is preceded by a cartilage element,

* Corresponding author

E-mail addresses: glimmt@wwu.edu (T. Glimm), RBhat@lbl.gov (R. Bhat), newman@nymc.edu (S.A. Newman).

which in turn arises from condensations of limb mesenchymal cells (Hall and Miyake, 2000). The condensation of mesenchymal cells can be observed in vitro in high-density micromass cultures. When precartilaginous mesenchymal cells are isolated from a developing chicken limb, dissociated and cultured at high densities on tissue culture plastic in serum-free conditions, they organize themselves into spot- or rod-like condensations of nearly uniform size and regularity of spacing surrounded by non-aggregated cells (Downie and Newman, 1994; Kiskowski et al., 2004; Christley et al., 2007). When packed into a limb bud ectodermal jacket the cells generate poorly formed, though discrete cartilaginous elements (Ros et al., 1994; Zwillig, 1964).

Aggregation results from random movement of cells occurring in an environment with local patches of increased adhesivity characterized by elevated levels of extracellular matrix (ECM) and adhesion molecules such as N-cadherin, NCAM, tenascin and fibronectin (Downie and Newman, 1995; Newman and Bhat, 2007). The determination of where the condensations form and where they do not, which determines the ultimate pattern of the skeleton, has proved to be a more difficult question.

The finding that regularly spaced condensations form from randomized cells in vitro, suggests that the mechanism of skeletal patterning is not dependent on stable gradients of diffusible molecules emanating from signaling centers as has been proposed in the form of the “positional information” hypothesis (Wolpert, 1969, 1989). Indeed, individual-based simulations of micromass cultures under experimentally constrained conditions (Kiskowski et al., 2004; Christley et al., 2007), analysis of the peculiarities of the limb skeletal patterns in certain mutant chicken embryos (Miura et al., 2006), and recently, examination of the response of skeletal pattern generation in mouse embryos in which Hox gene expression was manipulated in a semi-quantitative fashion (Sheth et al., 2012), all point to the underlying core mechanism of skeletogenesis being a reaction-diffusion-like process, as suggested earlier by Newman and Frisch (1979). This category of mechanism was originally discussed in chemical terms by Turing (1952), and in a biological context by Gierer and Meinhardt (1972), who characterized it as local autoactivation–lateral inhibition (LALI) (see Meinhardt and Gierer, 2000). The observation that the ECM molecule fibronectin is an important component of the condensation-associated adhesive patches and that one or more members of the TGF- β family of positively autoregulatory morphogens induces its synthesis, motivated mathematical and computational models of in vivo (Hentschel et al., 2004) and in vitro (Kiskowski et al., 2004; Christley et al., 2007) pattern formation, utilizing LALI mechanisms. (For exhaustive reviews on the mathematical models of limb pattern formation see Glimm et al., 2012; Newman et al., 2008; Zhang et al., 2013.)

The most general formulation of a Turing-type patterning process in limb bud mesenchyme is “morphodynamic” (in the sense of Salazar-Ciudad et al., 2003, in which cell–cell signaling and cell movement occur simultaneously), see Hentschel et al. (2004), Kiskowski et al. (2004) and Christley et al. (2007). However such a system is prohibitive to simulate in realistic geometries and thus a “morphostatic” approximation (where establishment of a stable “prepattern” of cell signals occurs on a faster time scale than cell movement, see Salazar-Ciudad et al., 2003) of the activator–inhibitor morphogen dynamics based on certain restrictive biological and mathematical assumptions (Alber et al., 2008) was used to explore some of its experimental, mutational and evolutionary properties (Zhu et al., 2010). It is unclear, however, to what extent this morphostatic assumption is justified in the developmental context. Moreover, the molecular identity of the putative LALI inhibitor in the TGF- β -fibronectin network has been elusive (Newman and Bhat, 2007).

Recently, in an attempt to clarify the identities of early acting determinants of precartilaginous condensations, Bhat et al. (2011)

showed that two members of a class of glycan-binding proteins called galectins appear at the sites of prospective condensation in the developing chicken limb before any previously described condensation mediators such as fibronectin. These galectins are CG (chicken galectin)-1A and CG-8 (see also Lorda-Diez et al., 2011). Ectopic CG-1A induced supernumerary condensation formation in vitro and digit formation in vivo, both of which were inhibited by CG-8. What distinguishes the interaction of these gene products from other experimentally elucidated LALI networks is a mutually positive feedback loop exerted by the proteins on each other's gene expression with the inhibitory effect exerted at a different biological level, protein–protein interaction (Bhat et al., 2011). In addition, CG-1A induces the expression of a shared counterreceptor. (A more detailed review is given in Section 2.1.) A relevant question is whether the demonstrated interactions were sufficient to give rise to the characteristic condensation pattern or if additional components or interactions are required.

The purpose of this paper is to construct a mathematical model that incorporates the interactions of CG-1A and CG-8 multilevel regulatory network to explore their ability to form spatial patterns of condensations. We verify that this mathematical model does indeed reproduce the experimental findings, and in the process, gives rise to a condensation-like pattern. The model provides additional crucial insights into the pattern formation from a physical perspective: we show that the limb skeletal patterning is a morphodynamic process (as opposed to morphostatic one) and is thus dependent on mesenchymal cell motility. We also confirm the predictive potential of the model by verifying experimentally an important in silico finding: that abrogation in the interaction of both chicken galectins to their counterreceptors results in loss of pattern formation. A number of explicit predictions of the model for further experimental tests are listed in Section 5 at the end of this paper.

The mathematical model and its experimental validation described below establish a novel “dynamical patterning module” (Newman and Bhat, 2008), a LALI-type mechanism for which cell movement is an intrinsic component. This mechanism underlies spatial patterning of the avian limb skeleton, but may also be relevant to the generation of other spot-like or rod-like biological patterns in animal development.

2. Materials and methods

2.1. Developmental model

In this section we present the key biological findings that we implement in our mathematical model in order to test their ability to give rise to spatial patterns characteristic of precartilaginous condensations in culture.

Biological assumptions motivated by the experimental findings:

1. Limb mesenchymal cells move randomly with a constant diffusion rate unless their surface adhesive properties change.
2. All cells produce CG-1A, CG-8 and their respective counterreceptors.
3. CG-1A induces CG-8 gene expression; CG-8 induces CG-1A gene expression.
4. CG-1A induces enhanced binding activity of the shared counterreceptor, presumably via upregulation of protein expression of the shared counterreceptor.
5. CG-1A promotes cell–cell adhesion in a cellular suspension in the order of minutes.
6. Cell movement continues but becomes confined within condensations.

Detailed experimental justifications for these biological assumptions are presented by Bhat et al. (2011). The following assertions

also come directly from experimental findings. But in contrast to the list above, instead of being explicitly incorporated in the model they are empirically valid outcomes that follow from the modeling assumptions (see Section 4.2). The following are thus “outputs” rather than “inputs” of the model.):

1. CG-1A and CG-8 are elevated in expression at prospective sites of condensation¹ in culture and in vivo.
2. CG-8 inhibits the cell–cell adhesion induced by CG-1A.
3. CG-1A promotes the formation of condensations: If CG-1A is added to cultures, condensation number and density increase (Fig. 1B).
4. CG-8 antagonizes the patterning of condensations: If CG-8 is added to cultures, condensation number and density decrease (Fig. 1C).

The exact molecular identity of the counterreceptors is presently not known; however, the extremely short time-scale of the adhesion inducing effects of CG-1A, and the inhibition by CG-8 of CG-1A-induced adhesion suggests that the two galectins have a common counterreceptor in addition to any unique ones. Correspondingly, the inhibition by CG-8 of condensations may thus be due to competition for binding to the shared counterreceptor with CG-1A. CG-8 is a tandem-repeat galectin and has two dissimilar CRDs with affinities to two different glycan moieties. Therefore CG-8 has at least two different counterreceptors. For simplicity we assume that there are two, and refer to them as the unique CG-8 counterreceptor and the shared (with CG-1A) counterreceptor. The unique CG-8 counterreceptor will also simply be referred to as “the CG-8 counterreceptor”, and the shared counterreceptor will also be referred to as “the CG-1A counterreceptor” or “CG-1A’s counterreceptors”, even though CG-8 can bind to it as well. CG-1A may also have a unique counterreceptor, but since experiments in this system do not provide any evidence for or against this, we will not consider it further in the models.

Studies carried out on the vertebrate homologs of CG-1A in other systems indicate that it has both intracellular and extracellular functions in different contexts (Gabijs, 2009). Given the short time course of the cell suspension aggregation experiments, it is a reasonable assumption that the two galectins act extracellularly with regard to mediation of condensation. We thus assume that they diffuse through the extracellular space and exert their patterning effects through their membrane-bound counterreceptors.

Further, we assume that it is through binding of CG-1A to its (shared) counterreceptor that the former enhances expression of its counterreceptor and of CG-8 and that the binding of CG-8 to its unique counterreceptor enhances expression of CG-1A; and finally, binding of CG-8 to the shared counterreceptor has no regulatory effect (other than the indirect one of making the binding site inaccessible to CG-1A). We also assume that in contrast to the case with CG-1A, the binding of CG-8 to either of its counterreceptors has no effect on their expression. The regulatory effects of the binding of a galectin to a counterreceptor are summarized in Fig. 2.

2.2. Experimental background

Materials and methods pertaining to the experimental model, i.e., limb mesenchymal micromass cultures, are elaborated in detail by Bhat et al. (2011). The following is a brief summary of the relevant procedures. Briefly, myoblast-free precartilaginous mesenchymal tissue was dissected from the distal 0.3 mm of Hamburger and Hamilton (1951) stage 24 leg or wing buds of 5-day fertilized White Leghorn chicken embryos (Moyer’s Chicks, Quakertown, PA) (Downie and Newman, 1994, 1995; Frenz et al., 1989a, 1989b). The cells were dissociated using TrypLE express solution (Gibco, Grand Island, NY) filtered through Nytex 20 μm monofilament nylon mesh (Tetco, Briarcliff Manor, NY), and cultured in serum-free medium at 2.5×10^5 cells per 10 μl spot.

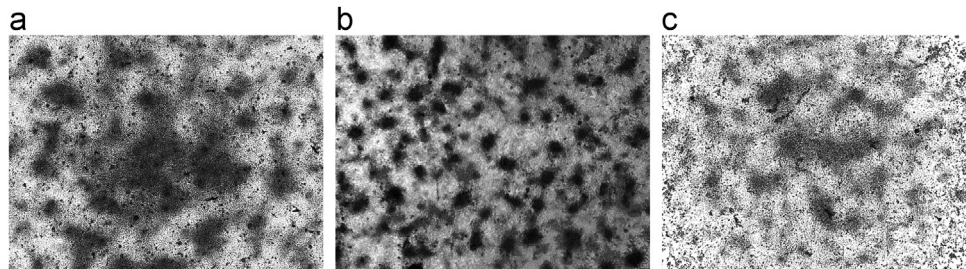


Fig. 1. Images of chondrogenic condensation patterns of leg cultures for three cases: control (a); added CG-1A (b); and added CG-8 (c). Note that the addition of CG-1A causes increased condensation numbers, with concomitant decrease in size as compared to the control; addition of CG-8 causes fewer condensations, with concomitant decrease in size.

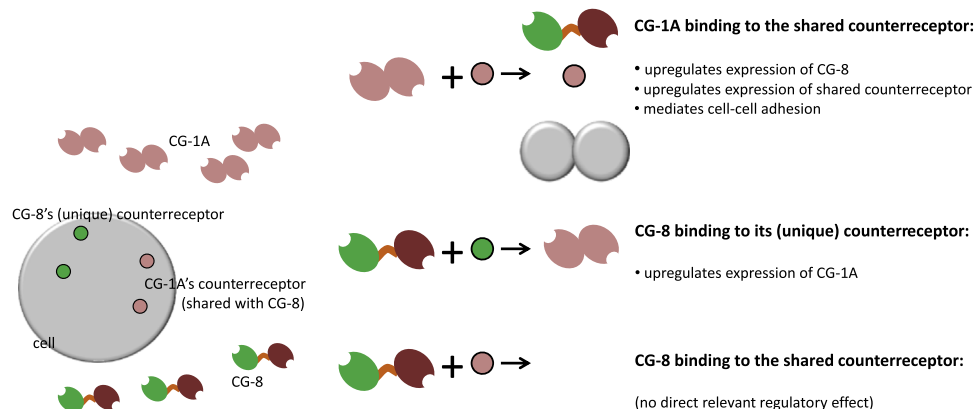


Fig. 2. Schematic representation of the galectin regulatory network: *Left*: graphical representation of matrix-bound galectins and their cell membrane-bound counterreceptors; *right*: schematic representation of the “minimal” regulatory network described in the text: the effects of galectins binding to counterreceptors.

Table 1
List of variables used in the model.

t	Time
\mathbf{x}	Location
$c_1^u = c_1^u(t, \mathbf{x})$	Concentration of freely diffusible CG-1A (that is, CG-1A not bound to counterreceptors on cell membranes)
$c_8^u = c_8^u(t, \mathbf{x})$	Concentration of freely diffusible CG-8 (that is, CG-8 not bound to counterreceptors on cell membranes)
$R = R(t, \mathbf{x}, c_1, c_8, c_8^1, \ell_1, \ell_8)$	Morphogenetic density with respect to the following variables: Volume, Concentr. c_1 of CG-1A bound to shared counterreceptors on cell membranes, Concentr. c_8^u of CG-8 bound to CG-8's unique counterreceptors on cell membranes, Concentr. c_8^1 of CG-8 bound to shared counterreceptors on cell membranes, Concentr. ℓ_1 of shared counterreceptors (not bound to galectins) on cell membranes, and Concentr. ℓ_8 of CG-8 counterreceptors (not bound to galectins) on cell membranes

2.3. Mathematical model

2.3.1. Variables and notation

In this section, we describe the complete mathematical model of the pattern formation mechanism. The model is based on the developmental model described in Section 2.1, specifically as summarized in Fig. 2.

The relevant variables are the cell densities, the concentrations of the counterreceptors, the concentrations of the freely diffusing galectins and those bound to their counterreceptors. Table 1 lists the variables and summarizes our notations.

Note that we have introduced morphogenetic density R as a generalized cell density depending on several variables representing various chemical concentrations besides time and space. A proper mathematical viewpoint is that $R(t, \mathbf{x}, c_1, c_8, c_8^1, \ell_1, \ell_8) d\mathbf{x} dc_1 dc_8^u dc_8^1 d\ell_1 d\ell_8$ is a time-dependent measure on the space $\mathbb{R}^n \times (\mathbb{R}_0^+)^5$, where \mathbb{R}_0^+ denotes the set of nonnegative reals and n is the number of spatial dimensions. More intuitively, $R(t, \mathbf{x}, c_1, c_8^u, c_8^1, \ell_1, \ell_8)$ can be roughly thought of as the number of cells at location \mathbf{x} and time t which have c_1 CG-1A molecules bound to shared counterreceptors on their membranes, c_8^u CG-8 molecules bound to CG-8 counterreceptor, c_8^1 CG-8 molecules bound to shared counterreceptor, ℓ_1 molecules of CG-1's counterreceptors, and ℓ_8 molecules of CG-8 counterreceptor.² For instance the cell density at a point \mathbf{x} at time t is given by the integral over the various concentrations:

Cell density at location \mathbf{x}

$$= \int_0^\infty \int_0^\infty \int_0^\infty \int_0^\infty \int_0^\infty R(t, \mathbf{x}, c_1, c_8, c_8^1, \ell_1, \ell_8) dc_1 dc_8^u dc_8^1 d\ell_1 d\ell_8$$

To write expressions as above in a more compact form, we introduce the following notation: we denote the integral over

¹ Strictly speaking, the elevated galectin concentrations are associated with “protocondensations,” subtle changes in cell-cell association that precede overt morphological condensations (Bhat et al., 2011). Since protocondensations provide the templates for the condensations themselves, for simplicity, the latter term will be used throughout this paper for the galectin-determined cell associations.

² Note on the mathematical notation: Here and elsewhere, the letter ℓ is used to denote various counterreceptor concentrations. The use of this letter refers to the fact that these counterreceptors have also been referred to as “ligands”.

the various concentration as

$$\int \dots dP = \int_0^\infty \int_0^\infty \int_0^\infty \int_0^\infty \int_0^\infty \dots dc_1 dc_8^u dc_8^1 d\ell_1 d\ell_8 \quad (2.1)$$

The total concentration of CG-1A at time t and location \mathbf{x} (bound to its counterreceptor or freely diffusible) is thus

$$c_1^u(t, \mathbf{x}) + \int c_1 \cdot R(t, \mathbf{x}, c_1, c_8, c_8^1, \ell_1, \ell_8) dP.$$

The morphogenetic density $R(t, \mathbf{x}, c_1, c_8, c_8^1, \ell_1, \ell_8)$ represents the confluence of biologically significant variables (the cell density and various counterreceptor concentrations, galectins) at any given point in space, and their time dependence. Alternatively, we could have introduced separate variables for the cell density and the various other components, but with that approach, the fact that counterreceptors are attached to the cells' plasma membranes would not be as straightforward to model. Additionally, our approach makes it possible to obtain detailed information about the distribution of counterreceptors, for instance the dynamics of the Gaussian distributions of the mutually shared counterreceptors on cell membranes. In Fig. 5 we demonstrate that in our model, the effect of higher condensation wavenumbers for increased initial CG-1A concentrations is due to an increase in the average concentration of shared counterreceptors (see also Fig. 6).

This approach has formal similarities to the equations for structured populations from the field of mathematical population biology (Thieme, 2003; Diekmann, 1999), where population densities depend on one or more structural parameters such as age, in addition to possibly a spatial dependence.

We note that in Section 4.3.1, we also obtain a “reduced model” under the assumption of fast counterreceptor dynamics. This is a system of reaction–diffusion equation involving a cell density as one of the variables. The reduced model displays many of the properties of the “full,” more complicated model; certain features of the full model are not reproduced by the reduced model, however.

2.4. The model

In the following, we write down the equations for the morphogenetic density R , and the equations for the freely diffusible (unbound) galectins c_1^u and c_8^u .

2.4.1. Equation for the morphogenetic density R

The equation for the morphogenetic density R takes into account the Brownian motion, cell–cell adhesion, binding and unbinding of galectins to counterreceptors, and changes in the counterreceptor concentrations on the cell membranes (through expression of counterreceptors and detachment of galectins from

Table 2
Explanation of terms in the morphogenetic density equation (2.2). A term with a bar over it (for example $\bar{\alpha}_1$) denotes a constant.

$D_R = const$	Cell diffusion coefficient
$\alpha = \bar{\alpha}_1 c_1^u \ell_1 - \bar{\alpha}_2 c_1$	Change in CG-1A bound to the shared counterreceptor: uptake at rate prop. to $c_1^u \ell_1$; random detachment
$\beta_8 = \bar{\beta}_{8,1} c_8^u \ell_8 - \bar{\beta}_{8,2} c_8^u$	Change in CG-8 bound to its own counterreceptor
$\beta_1 = \bar{\beta}_{1,1} c_8^u \ell_1 - \bar{\beta}_{1,2} c_8^1$	Change in CG-8 bound to the shared counterreceptor
$\gamma = \bar{\gamma}_1 \frac{c_1}{c_1 + c_1} - \bar{\gamma}_2 \ell_1$	Change in the shared counterreceptor: (Expression depends on CG-1A concentration; degradation)
$\delta = \bar{\delta}_1 - \bar{\delta}_2 \ell_8$	changes in CG-8 counterreceptor: (Expression is constant (independent of CG-8 concentration))

counterreceptors). The equation is as follows:

$$\begin{aligned} \frac{\partial R}{\partial t} = & \underbrace{D_R \nabla^2 R}_{\text{cell diffusion}} - \underbrace{\nabla \cdot (\mathbf{R}\mathbf{K}(R))}_{\text{cell-cell adhesion}} \\ & - \underbrace{\frac{\partial}{\partial c_1}(\alpha R) - \frac{\partial}{\partial c_8^8}(\beta_8 R) - \frac{\partial}{\partial c_8^1}(\beta_1 R)}_{\text{binding/unbinding of galectins to counterreceptors}} \\ & - \underbrace{\frac{\partial}{\partial \ell_1}[(\gamma - \alpha - \beta_1)R] - \frac{\partial}{\partial \ell_8}[(\delta - \beta_8)R]}_{\text{change in counterreceptors}} \end{aligned} \quad (2.2)$$

In the above equation, the terms in the formulas are summarized in Table 2. (A term with a bar over it (for example $\bar{\alpha}_1$) denotes a constant.)

For example, the term $\gamma - \alpha - \beta_1$ models the rate at which the membrane-bound concentration of the shared counterreceptors which are not bound to either galectin changes: the change is due to the expression of new counterreceptors by the cells and degradation (leading to the effective rate γ), the binding and unbinding of the counterreceptor to CG-1A (the rate α) and the binding and unbinding of the counterreceptor to CG-8 (the rate β_1). We assume simple mass action-type dependencies of the rates on the various concentrations. Note two crucial assumptions that are directly motivated by experimental results: the rate of expression of CG-1A counterreceptor depends on the concentration c_1 of bound CG-1A (see the formula for γ above); this dependence is modeled with a Michaelis–Menten term. In contrast, the expression of CG-8 counterreceptor is constant, and thus independent of the concentration of bound CG-8.

Finally, the cell–cell adhesion term is formulated based on the approach of Armstrong et al. (2006). Namely, we have

$$\begin{aligned} \mathbf{K}(R(t, \mathbf{x}, c_1, c_8^8, c_8^1, \ell_1, \ell_8)) \\ = \bar{\alpha}_K c_1 \iint_{D_{\rho_0}} \int \tilde{c}_1 \sigma(R(t, \mathbf{x} + \mathbf{r}, \tilde{c}_1, \tilde{c}_8^8, \tilde{c}_8^1, \tilde{\ell}_1, \tilde{\ell}_8)) d\tilde{P} \frac{\mathbf{r}}{|\mathbf{r}|} d^n r \end{aligned} \quad (2.3)$$

Here $\bar{\alpha}_K$ is a constant which represents the strength of the adhesion. The effective adhesion force on a cell at location \mathbf{x} depends on the product of the concentration of bound CG-1A on the cell and the concentration of bound CG-1A at locations $\mathbf{x} + \mathbf{r}$, where the distance vector \mathbf{r} varies over the n -dimensional ball $D_{\rho_0}(\mathbf{x})$ centered at \mathbf{x} , where we can consider from one to three spatial dimensions ($n = 1, 2, 3$). The radius ρ_0 is the “sensing” radius, which is a measure of the characteristic distance for adhesion; cells at distance greater than ρ do not contribute to the adhesion forces.

There are many possible choices for the function $\sigma(R)$, which describes the dependence of the adhesion forces on the cell density. The simplest choice is a proportionality assumption:

$$\sigma(R) = R \quad (2.4)$$

In this case, the contribution to the adhesion force from location $\mathbf{x} + \mathbf{r}$ is simply proportional to the concentration of bound CG-1A at that location. In this model, the cell density can in principle get arbitrarily large. To avoid this, one can take into account that above a certain density, the effective attractive forces due to cell–cell adhesion are balanced effectively by repulsive forces due to volume exclusion; that is, cells cannot be packed into arbitrarily small domains. This is implemented by a logistic form for the function σ , more precisely (Armstrong et al., 2006):

$$\sigma(R) = \frac{R_m}{R_m - R} R \max \left\{ 1 - \frac{1}{R_m} \int R dP, 0 \right\}. \quad (2.5)$$

Recall that $\int R dP$ is the total cell density, and so the above expression involves a volume constraint term. Here R_m is a constant that specifies the maximum cell density for adhesion and $\bar{R} < R_m$ is a characteristic cell density. The proportionality factor above is chosen such that the logistic term (2.5) has the same value as the linear term (2.4) if $R(t, \mathbf{x}, c_1, c_8^8, c_8^1, \ell_1, \ell_8)$ is

constant in time and spatially homogeneous, or more specifically if it has the form $R(t, \mathbf{x}, c_1, c_8^8, c_8^1, \ell_1, \ell_8) = \bar{R} \cdot \phi(c_1, c_8^8, c_8^1, \ell_1, \ell_8)$, where ϕ is some function.

Of course, many other functional forms for the expression $\sigma(R)$ are possible. We tested both the linear form (2.4) and the logistic form (2.5) in numerical simulations (see Section 4.2 and in particular, Section 4.2.5). We found that they both resulted in qualitatively very similar patterns, with the only difference being that for the logistic form, the density peaks were less high and the regions of low cell density between the peaks were less low. We generally used the linear term (2.4) in simulations, mostly because this avoids introducing another parameter, but see Section 4.2.5 for a more in-depth treatment.

A straightforwardly analogous expression of the flux density (2.3) is valid for one or three spatial dimensions.

Eq. (2.2) was considered in a spatial domain Ω (one-, two- or three-dimensional) with normal field $\mathbf{n}(\mathbf{x})$, $\mathbf{x} \in \partial\Omega$. It has the following initial and boundary conditions:

$$\text{Initial condition: } R(0, \mathbf{x}, c_1, c_8^8, c_8^1, \ell_1, \ell_8) = R_0(\mathbf{x}, c_1, c_8^8, c_8^1, \ell_1, \ell_8) \quad (2.6)$$

$$\text{Boundary conditions: } \frac{\partial R}{\partial \mathbf{n}} \Big|_{\mathbf{x}} = 0$$

$$\text{for } \mathbf{x} \in \partial\Omega, R|_{c_1=0} = R|_{c_8^8=0} = R|_{c_8^1=0} = R|_{\ell_1=0} = R|_{\ell_8=0} = 0. \quad (2.7)$$

This means that there are no (diffusive) flux conditions on the boundary of the spatial domain. (Alternatively, we also used periodic boundary conditions for the spatial domain in simulations, see Section 4.2.) We assume that the decay of $R(t, \mathbf{x}, c_1, c_8^8, c_8^1, \ell_1, \ell_8)$ in the non-temporal and non-spatial variables is fast enough so that the integrals $\int R dP$, $\int c_1 R dP$, etc. are all finite. The inflow boundary condition that R is zero when one of the concentrations of the various proteins is zero ensures that no new cells are created; indeed, only newly created cells can have zero protein concentrations on their membranes. Mathematically, the corresponding fact that the total cell mass is conserved is evident when Eq. (2.2) is integrated with respect to $d^{n\mathbf{x}}$ and dP . The boundary conditions then guarantee that the right-hand side is zero.

2.4.2. Equations for the free galectin concentrations

The equations for the free galectin concentrations c_1^u and c_8^u take into account the diffusion, degradation, binding to and detaching from counterreceptors, and secretion by cells. The equations are as follows:

$$\frac{\partial c_1^u}{\partial t} = \underbrace{D_1 \nabla^2 c_1^u + \bar{\nu}}_{\text{diffusion}} \underbrace{c_8^8 R dP}_{\text{pos. feedback of CG-8 on prod. of CG-1A}} - \underbrace{\int \alpha R dP}_{\text{binding of CG-1A to its counterreceptor}} - \underbrace{\bar{\pi}_1 c_1^u}_{\text{degradation}} \quad (2.8)$$

$$\frac{\partial c_8^u}{\partial t} = \underbrace{D_8 \nabla^2 c_8^u + \bar{\mu}}_{\text{diffusion}} \underbrace{\int c_1 R dP}_{\text{pos. feedback of CG-1A on prod. of CG-8}} - \underbrace{\int \beta_1 R dP}_{\text{binding of CG-8 to counterreceptors}} - \underbrace{\int \beta_8 R dP}_{\text{degradation}} - \underbrace{\bar{\pi}_8 c_8^u}_{\text{degradation}} \quad (2.9)$$

All terms in the above equations not defined in previous sections are constants.

Again, we have boundary and initial conditions for these equations, which here are

$$\text{Initial condition: } c_1^u(0, \mathbf{x}) = c_{1,0}^u(\mathbf{x}), \quad c_8^u(0, \mathbf{x}) = c_{8,0}^u(\mathbf{x}) \quad (2.10)$$

$$\text{Boundary conditions: } \frac{\partial c_1^u}{\partial \mathbf{n}} \Big|_{\mathbf{x}} = \frac{\partial c_8^u}{\partial \mathbf{n}} \Big|_{\mathbf{x}} = 0 \quad \text{for } \mathbf{x} \in \partial\Omega \quad (2.11)$$

Again, in simulations we also use periodic boundary conditions instead of the no-flux Neumann conditions (see Section 4.2).

3. Analysis and model simplifications

We now describe some analysis and simplification of the system of Eqs. (2.2), (2.8) and (2.9). Mathematically, one source of difficulties is the nonlocal term $\mathbf{K}(R)$ given in (2.3). From a modeling point of view, it has to be noted that the parameter space is quite large with 16 parameters. As is typical for models in developmental biology, few of the parameters can be determined with any accuracy. In several cases, such as expression rates, little is known about even the order of magnitude.

We first derive a simpler set of equations based on the assumption of fast counterreceptor binding and unbinding. Specifically, we assume that these processes happen on a faster time scale than the secretion of proteins and changes in the cell density due to cell motion. This assumption is well supported by data. We then non-dimensionalize these equations to arrive at the “full” model equations. We list the resulting parameters, their meanings and some approximate values in Table 4.

3.1. Fast counterreceptor binding and unbinding

Note that the morphogenetic density $R = R(t, \mathbf{x}, c_1, c_8^s, c_1^s, \ell_1, \ell_8)$ depends on five different concentrations, and so together with one to three spatial dimensions, this makes the problem relatively high dimensional. This poses, in particular, problems for the numerical solution of the system described by the Eqs. (2.2), (2.8) and (2.9).

In order to reduce the dimensionality, we can separate “fast” and “slow” variables. Namely, we make the assumption that binding of galectins to counterreceptors happens on a faster time scale than significant redistributions in protein abundance. This is a common assumption in mathematical models of complex multi-component systems. It may or may not be true, but at least it is an explicit feature of the model that can be tested. We define the total concentration of CG-1As counterreceptors (whether unbound or bound to CG-1A or CG-8) to be

$$T_1 = c_1 + c_8^1 + \ell_1. \tag{3.1}$$

Similarly, the total concentration of CG-8 counterreceptor is

$$T_8 = c_8^s + \ell_8. \tag{3.2}$$

Now, the binding and unbinding of galectins to counterreceptors happen on a faster time scale than changes in the patterns of protein concentrations and the cell density. This means that the variables $c_1, c_8^1, \ell_1, c_8^s$ and ℓ_8 are “fast” variables, whereas T_1 and T_8 , which only depend on the production rates of the counterreceptors and not of the binding and unbinding, are “slow” variables. So the rates γ and δ are in some sense “small” compared to the rates α, β_1 and β_8 .

We will use these observations to simplify the model equations without giving a mathematically strictly rigorous derivation. First we introduce the transformation in the concentration space:

$$(c_1', c_8^1, c_8^s, T_1, T_8) = (c_1, c_8^1, c_8^s, c_1 + c_8^1 + \ell_1, c_8^s + \ell_8)$$

It is straightforward to verify that this transformation satisfies

$$dc_1' dc_8^1 dc_8^s dT_1 dT_8 = dc_1 dc_8^1 dc_8^s d\ell_1 d\ell_8.$$

The system (2.2), (2.8) and (2.9) now appears with these new variables, dropping the primes for better readability:

$$\frac{\partial R}{\partial t} = D_R \nabla^2 R - \nabla \cdot (\mathbf{R}\mathbf{K}(R)) - \frac{\partial}{\partial c_1} (\alpha R) - \frac{\partial}{\partial c_8^s} (\beta_8 R)$$

$$- \frac{\partial}{\partial c_8^1} (\beta_1 R) - \frac{\partial}{\partial T_1} (\gamma R) - \frac{\partial}{\partial T_8} (\delta R)$$

$$\frac{\partial c_1^u}{\partial t} = D_1 \nabla^2 c_1^u + \bar{\nu} \int c_8^s R dP - \int \alpha R dP - \bar{\pi}_1 c_1^u$$

$$\frac{\partial c_8^u}{\partial t} = D_8 \nabla^2 c_8^u + \bar{\mu} \int c_1 R dP - \int \beta_1 R dP - \int \beta_8 R dP - \bar{\pi}_8 c_8^u.$$

Here we have used the notation $dP = dc_1 dc_8^1 dc_8^s dT_1 dT_8$.

The fact that the variables c_1, c_8^1 and c_8^s are “fast” means that we can effectively consider solutions of the form:

$$R(t, \mathbf{x}, c_1, c_8^1, c_8^s, T_1, T_8) = R(t, \mathbf{x}, T_1, T_8) \delta(\tilde{c}_1 - c_1) \delta(\tilde{c}_8^s - c_8^s) \delta(\tilde{c}_1^1 - c_8^1),$$

where δ denotes the Dirac delta function, and $\tilde{c}_1 = \tilde{c}_1(t, \mathbf{x}, T_1, T_8)$, $\tilde{c}_8^s = \tilde{c}_8^s(t, \mathbf{x}, T_1, T_8)$ and $\tilde{c}_1^1 = \tilde{c}_1^1(t, \mathbf{x}, T_1, T_8)$ are certain equilibrium concentrations. Thus the above equation essentially is a quasi-steady state approximation. (In Appendix A, we provide an argument for the plausibility of this form by proving for a simplified version of (2.2) that solutions converge to a point measure (Dirac measure) in the sense of weak convergence of measures as $t \rightarrow \infty$. This is not a mathematically rigorous result for (2.2), which would be outside the scope of this paper, but we plan to address this in a future publication.) These equilibria can be determined through the relations:

$$\alpha = 0, \quad \beta_8 = 0, \quad \beta_1 = 0,$$

along with (3.1) and (3.2). Dropping the tildes, this yields

$$c_1 = \frac{\bar{\alpha}_1}{\bar{\alpha}_2} c_1^u \ell_1, \quad c_8^1 = \frac{\bar{\beta}_{1,1}}{\bar{\beta}_{1,2}} c_8^u \ell_1, \quad c_8^s = \frac{\bar{\beta}_{8,1}}{\bar{\beta}_{8,2}} c_8^u \ell_8, \tag{3.3}$$

with

$$\ell_1 = \frac{T_1}{1 + \bar{\alpha}_1 c_1^u / \bar{\alpha}_2 + \bar{\beta}_{1,1} c_8^u / \bar{\beta}_{1,2}}, \quad \ell_8 = \frac{T_8}{1 + \bar{\beta}_{8,1} c_8^u / \bar{\beta}_{8,2}}. \tag{3.4}$$

Thus the system (2.2), (2.8) and (2.9) can be simplified to the following system for $R(t, \mathbf{x}, T_1, T_8)$, $c_1^u(t, \mathbf{x})$ and $c_8^u(t, \mathbf{x})$:

$$\frac{\partial R}{\partial t} = D_R \nabla^2 R - \nabla \cdot (\mathbf{R}\mathbf{K}(R)) - \frac{\partial}{\partial T_1} (\gamma R) - \frac{\partial}{\partial T_8} (\delta R) \tag{3.5}$$

$$\frac{\partial c_1^u}{\partial t} = D_1 \nabla^2 c_1^u + \bar{\nu} \int_0^\infty \int_0^\infty c_8^s(T_8) R dT_1 dT_8 - \bar{\pi}_1 c_1^u \tag{3.6}$$

$$\frac{\partial c_8^u}{\partial t} = D_8 \nabla^2 c_8^u + \bar{\mu} \int_0^\infty \int_0^\infty c_1(T_1) R dT_1 dT_8 - \bar{\pi}_8 c_8^u. \tag{3.7}$$

with

$$\begin{aligned} \mathbf{K}(R(t, \mathbf{x}, T_1, T_8)) \\ = \bar{\alpha}_K c_1(T_1) \iint_{D_{r_0}} \int_0^\infty \int_0^\infty c_1(\tilde{T}_1) \sigma(R(t, \mathbf{x} + \mathbf{r}, \tilde{T}_1, \tilde{T}_8)) d\tilde{T}_1 d\tilde{T}_8 \frac{\mathbf{r}}{|\mathbf{r}|} d^n r. \end{aligned} \tag{3.8}$$

Here $\sigma(R)$ has either the linear form (2.4) or the logistic form (2.5). In all these equations, we have used the relations (3.3) and (3.4). To better stress these dependencies we wrote $c_1(T_1)$ and $c_8^s(T_8)$. (These variables also depend on $c_1^u(t, \mathbf{x})$ and $c_8^u(t, \mathbf{x})$, but these dependencies are not explicitly indicated.)

3.2. Non-dimensionalization

We now non-dimensionalize Eqs. (3.5)–(3.7). To this end, we define the non-dimensional time, space, and various concentrations via

$$t^* = t/\hat{t}, \quad \mathbf{x}^* = \mathbf{x}/\hat{\lambda}, \quad T_1^* = T_1/\hat{T}_1,$$

$$T_8^* = T_8/\hat{T}_8, \quad (c_1^u)^* = c_1^u/\hat{c}_1^u, \quad (c_8^u)^* = c_8^u/\hat{c}_8^u, \quad R^* = R/\hat{R}.$$

Here the constant \hat{t} is a time scale, $\hat{\lambda}$ is a spatial scale, and $\hat{T}_1, \hat{T}_8, \hat{c}_1^u$ and \hat{c}_8^u are typically concentrations. Our choices are summarized in Table 3.

The scale of the morphogenetic density is given by

$$\hat{R} = \frac{1}{\hat{T}_1 \hat{T}_8 \hat{\lambda}} \int \int_0^\infty \int_0^\infty R dT_1 dT_8 d^n x$$

Note that the integral on the right is time-independent, as can be seen by integrating (3.5) with respect to $d^n x dT_1 dT_8$ and using

integration by parts and the boundary conditions. The above definition scales the total cell mass to 1.

We also assume in the following that the diffusion coefficients for the two galectins are the same; that is $D_1 = D_8$.

After non-dimensionalization, we obtain the following non-dimensional equations, where we dropped the stars on non-dimensional variables:

$$\frac{\partial R}{\partial t} = d_R \nabla^2 R - \nabla \cdot (R \mathbf{K}(R)) - \frac{\partial}{\partial T_1} (\tilde{\gamma}(c_1^u, c_8^u, T_1) R) - \frac{\partial}{\partial T_8} (\tilde{\delta}(c_8^u, T_8) R) \quad (3.9)$$

$$\frac{\partial c_1^u}{\partial t} = \nabla^2 c_1^u + \tilde{\nu} \int_0^\infty \int_0^\infty c_8^u R dT_1 dT_8 - c_1^u \quad (3.10)$$

$$\frac{\partial c_8^u}{\partial t} = \nabla^2 c_8^u + \tilde{\mu} \int_0^\infty \int_0^\infty c_1 R dT_1 dT_8 - \tilde{\pi}_8 c_8^u. \quad (3.11)$$

with

$$c_8^u = c_8^u(t, \mathbf{x}, T_8) = \frac{c_8^u T_8}{1 + c_8^u} \quad (3.12)$$

$$c_1 = c_1(t, \mathbf{x}, T_1) = \frac{c_1^u T_1}{1 + f c_8^u + c_1^u} \quad (3.13)$$

$$\tilde{\gamma}(c_1^u, c_8^u, T_1) = \left(\frac{2c_1^u}{c_1^u T_1 + \tilde{c}_1} - \tilde{\gamma}_2 \right) \frac{T_1}{c_1^u + f c_8^u + 1} \quad (3.14)$$

Table 3
Scales for the non-dimensionalization.

Dimensionless parameter	Value	Explanation
$\hat{t} = \frac{1}{\pi_1}$	Order of days	Time scale given by degradation of CG-1A
$\hat{x} = \sqrt{D_1 \hat{t}}$	Order of 0.1–1 mm	Spatial scale given by diffusion of CG-1A ^a
$\hat{T}_1 = \tilde{\gamma}_1 \hat{t} / 2$	Unknown	Scale for CG-1A counterreceptor concentrations
$\hat{T}_8 = \tilde{\delta}_1 \hat{t}$	Unknown	Scale for CG-8 counterreceptor concentrations
$\hat{c}_1^u = \frac{\bar{\alpha}_2}{\bar{\alpha}_1}$	Unknown	Scale for CG-1A concentrations
$\hat{c}_8^u = \frac{\bar{\beta}_{8,2}}{\bar{\beta}_{8,1}}$	Unknown	Scale for CG-1A concentrations

^a See Section 4.3 for evidence that the pattern-forming capability of the model is robust across a wide range of diffusion coefficient values.

Table 4
Table of parameters in the system of Eqs. (3.9)–(3.11).

Scale	Value	Explanation
$\tilde{\alpha}_K = \hat{t}(\hat{T}_1)^3 \hat{T}_8 \hat{R} \tilde{\alpha}_K$	Unknown	Related to cell–cell adhesion strength
$r_0 = \frac{\rho_0}{\hat{x}}$	Order of 10^{-2}	Interaction radius for cell–cell adhesion
$\tilde{\delta}_2 = \tilde{\delta}_2 \hat{t}$	Unknown	Related to degradation of CG-8 counterreceptor
$\tilde{\gamma}_2 = \tilde{\gamma}_2 \hat{t}$	Unknown	Ratio of degradation/production rate of CG-1A counterreceptor
$\tilde{c}_1 = \frac{\tilde{c}_1}{\hat{T}_1}$	Unknown	Parameter in Michaelis–Menten term describing expression of CG-1A counterreceptor
$f = \frac{\bar{\beta}_{1,1} \bar{\beta}_{8,2}}{\bar{\beta}_{1,2} \bar{\beta}_{8,1}}$	< 1, order unknown	Related to the relative rates at which CG-8 binds to its own and to CG-1A counterreceptor
$d_R = \frac{D_R}{D_1}$	<< 1	Cell diffusion coefficient
$\tilde{\pi}_8 = \frac{\pi_8}{\pi_1}$	≈ 1	Ratio of degradation rates of CG-1A and CG-8
$\tilde{\nu} = \nu \hat{t} \hat{R} (\hat{T}_8)^2 \hat{T}_1 \hat{x}$	Unknown	Related to secretion rate of CG-1A
$\tilde{\mu} = \mu \hat{t} \hat{R} \hat{T}_8 (\hat{T}_1)^2 \hat{x}$	Unknown	Related to secretion rate of CG-8

$$\tilde{\delta}(c_8^u, T_8) = 1 - \tilde{\delta}_2 \frac{T_8}{1 + c_8^u} \quad (3.15)$$

$$\mathbf{K}(R(t, \mathbf{x}, T_1, T_8)) = \tilde{\alpha}_K c_1(t, \mathbf{x}, T_1) \int_0^\infty \int_0^\infty \int_{D_{r_0}(\mathbf{x})} c_1(t, \mathbf{s}, \hat{T}_1) \tilde{\sigma}(R(t, \mathbf{s}, \hat{T}_1, \hat{T}_8)) \frac{\mathbf{s}}{|\mathbf{s}|} ds d\hat{T}_1 d\hat{T}_8 \quad (3.16)$$

Here we can either use a linear or logistic form for $\tilde{\sigma}$ in the expression for the adhesion flux, as indicated in (2.4) and (2.5), respectively, that is

$$\tilde{\sigma}(R) = R \text{ or } \quad (3.17)$$

$$\tilde{\sigma}(R) = \frac{\tilde{R}_m}{\tilde{R}_m - \tilde{R}} R \max\left(1 - \frac{1}{\tilde{R}_m} \int_0^\infty \int_0^\infty R dT_1 dT_8, 0\right) \text{ with } \tilde{R}_m = \frac{R_m}{\tilde{R}}, \quad \tilde{R} = \frac{\bar{R}}{\tilde{R}}. \quad (3.18)$$

We will mostly use the linear form for $\tilde{\sigma}$ in the simulations below, but see Section 4.2.5 for more details. In (3.16), D_{r_0} denotes a disk of radius r_0 centered at 0 (in two spatial dimensions), or, analogously, an interval in one dimension, or a ball in three dimensions.

The parameters appearing in the model are summarized in Table 4. A determination of the (formal) steady state of the system of Eqs. (3.9)–(3.11) is presented in Appendix B.

4. Results

Our results are divided into four subsections. In the first, we present experimental results that validate two biological assumptions of the mathematical model presented here that were not part of the study of Bhat et al. (2011), which provides the main empirical basis of the model. In the second subsection, we describe the initial simulation results of the model. These concur with our experimental conclusions concerning the mechanistic role of CG-1A and CG-8 in digit morphogenesis and patterning: CG-1A induces condensation formation and CG-8 acts as a mainly inhibitory regulator of condensation number and spacing. In the third subsection, we analyze the robustness of the model's account of the culture phenotypes. In the fourth subsection we demonstrate mathematically the morphodynamic (Salazar-Ciudad et al., 2003, sensu) nature of the two-galectin multiscale network. That is, cell–cell signaling and cell movement are involved simultaneously and inextricably in the described network motif, making it a unusual “dynamical patterning module” (Newman and Bhat, 2008).

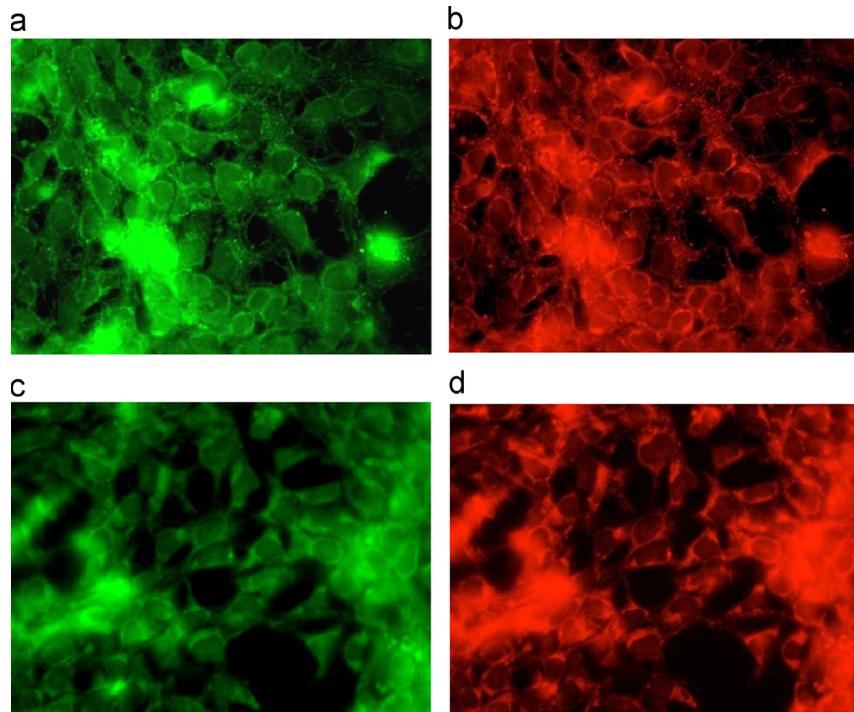


Fig. 3. CG-1A and CG-8 are predominantly localized on the surface of precartilaginous limb mesenchymal cells. Microscopic field in a 2-day high-density micromass culture showing indirect immunolocalization for CG-1A in precartilaginous limb mesenchymal cells (a) and staining of membrane-specific fluorescent dye Cell Mask (b). Microscopic field in a 2-day high density micromass culture showing indirect immunolocalization for CG-8 in precartilaginous limb mesenchymal cells (c) and the staining of membrane-specific fluorescent dye Cell Mask (d). Both CG-1A and CG-8 colocalize with Cell Mask suggesting a membrane-specific cellular distribution of the two chicken galectins. Images (a–d) are at same magnification and were photographed with a $63\times$ oil objective.

4.1. Experimental basis of additional assumptions of the model

As indicated above, the bulk of the empirical basis for the mathematical model is presented in the study of [Bhat et al. \(2011\)](#). In this section, we present data supporting two additional assumptions for our mathematical model which were not part of that study, namely that (a) the counterreceptors to which CG-1A and CG-8 bind on the limb precartilaginous mesenchymal cells are located on the cells' plasma membranes, and (b) that the production of the shared counterreceptor for CG-1A and CG-8 is under the positive control of CG-1A, whereas, in contrast, the production of CG-8's specific counterreceptor is not under the control of CG-8.

4.1.1. Cellular localization of CG-1A and CG-8

In order to observe localization of galectins within limb mesenchyme undergoing pattern formation, leg bud micromass cultures were fixed after 3 days. Separate sets of cultures were stained with antibodies against CG-1A and CG-8. To visualize membranes, the cultures were co-stained with the plasma membrane-specific dye Cell Mask (Invitrogen). Both CG-1A and CG-8 proteins were found to be predominantly localized to the cell surface of the mesenchymal cells ([Fig. 3](#)). Strong localization of CG-1A was also observed in the mesh-like ECM that the cells secrete while organizing themselves into condensations.

4.1.2. Effect of CG-8 on its counterreceptor

Limb bud micromasses were cultured in serum-free defined medium with and without addition of exogenous CG-8 for 2 days. After fixation, the cultures were treated with biotinylated CG-8, which has affinity for the counterreceptors of CG-8 ([Bhat et al., 2011](#)). While micromass cultures pretreated with CG-1A show higher localization of CG-1A counterreceptors than controls ([Bhat et al., 2011](#)), pretreating cultures with CG-8 had no effect on the localization of CG-8 counterreceptors (see [Fig. S4](#) in the Supplementary Material).

4.2. Analysis and simulation results

We now discuss the behavior of the system (3.9)–(3.11) by means of a numerical exploration. The parameters are summarized in [Table 4](#). Unfortunately, many values of the parameters are unknown, even their orders of magnitude. We thus concentrated on qualitative questions for this study rather than trying to match results quantitatively.

As indicated before, the goal of our study is to define the role of galectins in the core mechanism of pattern formation in the micromass experiments of [Bhat et al. \(2011\)](#). In particular, this includes a possible explanation of the apparent paradox that while CG-1A and CG-8 form a positive feedback loop, they have opposite effects on cell condensation if added to the micromass experiments (or injected into limb buds): while CG-1A enhances condensations, CG-8 is an inhibitor of condensations.

Our approach is two-fold: we first address the question of whether the model can display some of the key experimental results, listed below. As a proof of principle, this would be evidence that the key assumptions concerning the regulatory galectin network which form the basis of the model, as described in [Section 2.1](#), are sufficient to explain essential experimental findings. This proof of principle is the content of this subsection. The second step is then to use the model to make predictions which can in principle be tested experimentally, and also to conceptually specify the pattern forming mechanism in the model; that is to “back translate” the modeling results from a mathematical description to a verbal one. This last step is done in [Section 4.3](#).

For the first step, the proof of principle that the model can indeed explain key findings, we focused on the following three questions:

1. In the control case, can the system produce patterns in the cell density as observed in experiments?
2. When CG-1A is added, does the number of condensations increase, and under what conditions is this the case?

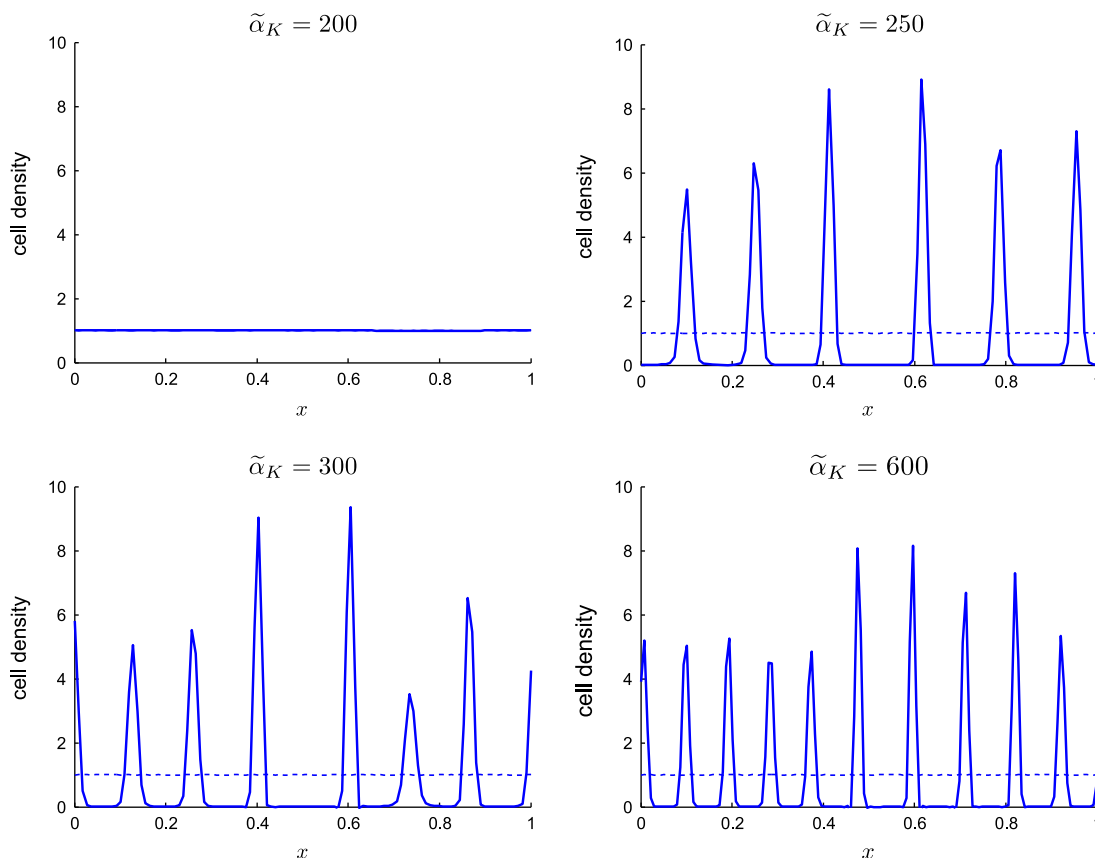


Fig. 4. Plots of the total spatial cell density $\iint R(t, x, T_1, T_8) dT_1 dT_8$ at times $t=0$ and $t=1$ for different values of the cell–cell adhesion constant $\tilde{\alpha}_K$. Other values are $r_0 = 0.04, \tilde{\delta}_2 = 1, \tilde{\gamma}_2 = 1, \tilde{c}_1 = 1, f = 0.8, d_R = 0.04, \tilde{\pi}_8 = 1, \tilde{\nu} = 0.8, \tilde{\mu} = 2$. Initial distributions are dashed, distributions at $t=1$ are solid. The initial cell distributions have small amplitude random noise added, which is not visible due to the scale of the vertical axis. For sufficiently small $\tilde{\alpha}_K$, no spatial patterns are produced (plot $\tilde{\alpha}_K = 200$). As $\tilde{\alpha}_K$ is increased, periodic patterns appear. The number of condensations (peaks) increases with $\tilde{\alpha}_K$ as illustrated. (Note that periodic boundary conditions are used, so that the positions $x=0$ and $x=1$ denote the same physical point.)

3. When CG-8 is added, does the number of condensations decrease, and under what conditions is this the case?

We demonstrate the capabilities of the model to reproduce the effects (1)–(3) above, but only conducted a somewhat limited search of parameter space owing to the large number of parameters. After illustrating that the system can reproduce these experimental results, we use a combination of analysis and further numerical simulation to investigate the basic mechanisms of this pattern formation.

4.2.1. Approach

To investigate the questions listed above, we numerically computed the solutions to (3.9)–(3.11) for different values of the parameters listed in Table 4. We used the one-dimensional interval $(0, 1)$ as the spatial domain with periodic boundary conditions for the morphogenetic density R and the galectin concentrations c_1^u and c_8^u . A Lax–Friedrich scheme was used to solve the equations numerically. As initial conditions for the control case, we chose the spatially homogeneous steady state concentrations \bar{c}_1^u and \bar{c}_8^u for $c_1^u(t, x)$ and $c_8^u(t, x)$ as given in Appendices B.1 and B.2, respectively. For the morphogenetic density $R(t, x, T_1, T_8)$, we chose the (multivariate normal) distribution:

$$R(t, x, T_1, T_8) = C \exp(-(T_1 - \bar{T}_1)^2 / \sigma_1) \exp(-(T_8 - \bar{T}_8)^2 / \sigma_8) \text{ with} \\ C = \left(\int_0^\infty \int_0^\infty \exp(-(T'_1 - \bar{T}_1)^2 / \sigma_1) \exp(-(T'_8 - \bar{T}_8)^2 / \sigma_8) dT'_1 dT'_8 \right)^{-1}, \quad (4.1)$$

with the steady state values for the counterreceptors of CG-1A and CG-8, \bar{T}_1 and \bar{T}_8 , given by Eqs. B.4 and B.3, respectively. (The Gaussian distributions in T_1 and T_8 with variances $\sigma_1/2, \sigma_8/2$ can be considered as perturbations around the steady state $R(t, \mathbf{x}, T_1, T_8) = \delta(T_1 - \bar{T}_1) \delta(T_8 - \bar{T}_8)$, where δ denotes the Dirac delta function.) Additionally, we added random spatial noise to the value of $R(t, x, T_1, T_8)$. For the function $\tilde{\sigma}$ in the adhesion flux (3.16), we used the linear form $\tilde{\sigma}(R) = R$ unless noted otherwise; see however Section 4.2.5.

To simulate the situations in questions (2) and (3) above, we increase the initial concentrations for c_1^u and c_8^u , respectively, while keeping the other unchanged relative to the “control” case.

4.2.2. The system can produce spontaneously emerging spatial patterns in the cell density

We first present evidence that the system (3.9)–(3.11) can produce spatial patterns in the morphogenetic density $R(t, x, T_1, T_8)$ for a wide range of parameters. While we will discuss the mechanism for this in Section 4.3 in depth, we also demonstrate that the cell–adhesion flux term $-\nabla \cdot (R\mathbf{K}(R))$ in (3.9) plays a crucial role here. This is similar to the formation of cell clusters in models of populations of cells with uniform adhesive properties (Armstrong et al., 2006). For this mechanism, it is important that the adhesive flux term $\mathbf{K}(R)$ in (3.16) be large enough. To illustrate this, consider Fig. 4, which shows the distribution of the cell density $\int_0^\infty \int_0^\infty R(t, x, T_1, T_8) dT_1 dT_8$ for four different values of the cell–cell adhesion constant $\tilde{\alpha}_K$.

This cell–cell adhesion constant $\tilde{\alpha}_K$ represents a measure of the strength of adhesion mediated by CG-1A. Below a certain threshold for $\tilde{\alpha}_K$, no pattern appears. As $\tilde{\alpha}_K$ is increased, a characteristic pattern of peaks representing condensations appears. The number of such condensations increases with $\tilde{\alpha}_K$.

For a further investigation of the subset of parameters which allows for pattern formation capabilities, see Section 4.3, where we derive a simplified system we term the “reduced system”. This system displays some of the key behaviors of the “full system” (3.9)–(3.11), but has the advantage that some analytic methods such as a linear stability analysis are possible. See in particular Fig. 12 which shows the region in $\tilde{c}_1 \tilde{\alpha}_K$ parameter space where the reduced system can produce patterns. More specifically, the gray region corresponds to points in parameter space where there is a wavenumber k with a corresponding positive temporal growth rate. As can be seen if we fix \tilde{c}_1 , then for large enough α_K , the system can produce patterns.

4.2.3. Effect of increased values for the initial CG-1A concentrations

We next investigate what happens if the initial concentration of freely diffusible CG-1A, $c_1^u(t, x)$, is taken to be larger than the equilibrium concentration \bar{c}_1^u .

By inspection of Eqs. (3.9)–(3.11), this leads to kinetics terms in $\partial c_8^u / \partial t$ being positive, and so the diffusible CG-8 concentration $c_8^u(t, x)$ increases, whereas correspondingly the diffusible CG-1A concentration $c_1^u(t, x)$ decreases, at least for some time. Most important though is the effect on the cell adhesion flux $RK(R)$ as given in (3.16). Note that the increase in the diffusible CG-1A concentration $c_1^u(t, x)$ leads to an increase in the number of CG-1A counterreceptors bound to CG-1A, $c_1(T_1)$, and thus an increase in the

adhesion flux $RK(R)$ compared to the “control” case. Very roughly speaking, this increase is equivalent to an increase in the cell–cell adhesion coefficient $\tilde{\alpha}_K$. One thus expects an increase in the number of condensations, similar to the effect of increasing $\tilde{\alpha}_K$ as illustrated in Fig. 4. (One should note that $c_1^u(t, x)$ is initially decreasing as explained above, and so that $RK(R)$ is decreasing in time, at least initially; however this decrease is typically slow enough that the spatial pattern in the cell density forms with significantly increased adhesion flux compared to the “control” case.)

Fig. 5 shows a typical plot of the resulting cell distribution for different levels of increased CG-1A. The calculated effect of increased CG-1A on CG-1A counterreceptors is to cause the average number of these counterreceptors per cell to increase approximately linearly over time (Fig. 6). This is an experimentally testable prediction of the model.

The above discussion can be summed up as follows: if levels of CG-1A are increased, the net effect is that more CG-1A counterreceptors are bound to CG-1A, leading to stronger cell–cell adhesion, which again leads to more cell condensations.

4.2.4. Effect of increased values for the initial CG-8 concentration

We now investigate what happens if the initial concentration of CG-8, $c_8^u(t, x)$, is taken to be larger than the equilibrium concentration \bar{c}_8^u .

Intuitively it is less clear what happens in this case. On the one hand, this should lead to a decrease in the percentage of CG-1A counterreceptors which are bound to CG-1A molecules, as CG-8 molecules will compete with CG-1A counterreceptors for the shared counterreceptors. This effect alone would lead to a decrease in cell–cell adhesion and fewer condensations. On the other hand,

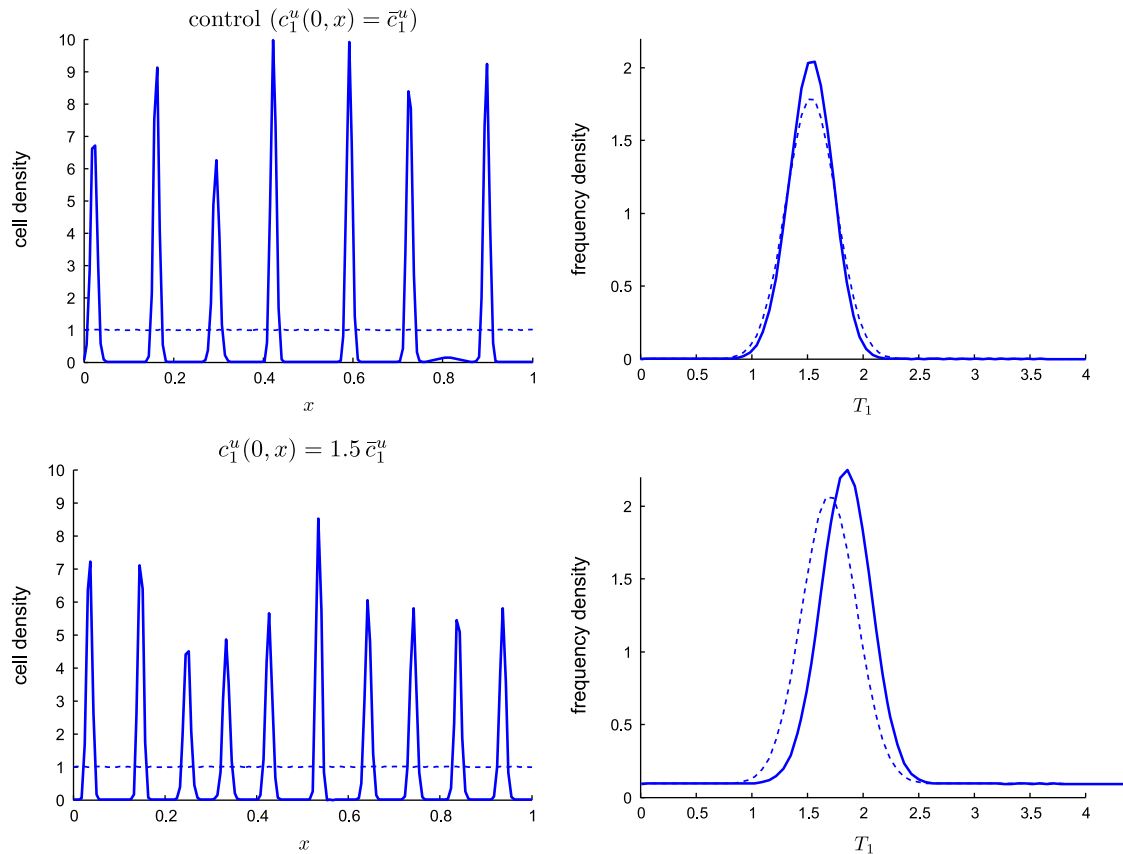


Fig. 5. An illustration of the effect of an increased initial CG-1A concentration. Left column: plots of the cell density $\iint R(t, x, T_1, T_8) dT_1 dT_8$ at times $t=0$ and $t=1$ for different initial values of the freely diffusible CG-1A concentration $c_1^u(t, x)$. Right column: frequency distribution of the CG-1A counterreceptor molecules on cell membranes corresponding to the cell density on the left. (For instance, in the “control” case, T_1 distribution is approximately Gaussian with mean $T_1 = \bar{T}_1 \approx 1.5$.) Initial distribution is dashed, distribution at $t=1$ is solid. Parameter values were as in Fig. 4 with $\tilde{\alpha}_K = 400$. The figure illustrates that increasing the initial CG-1A concentration leads to a pattern with larger wavenumber, i.e., a higher numbers of condensations. Note that the mean number of CG-1A counterreceptors T_1 increases (left column).

an increase in CG-8 also leads to increased production of CG-1A and therefore potentially the latter's counterreceptors. Thus, while the percentage of shared counterreceptors bound to CG-1A is lowered, this effect may be mitigated and in fact canceled out by an increase in the total number of the shared counterreceptors.

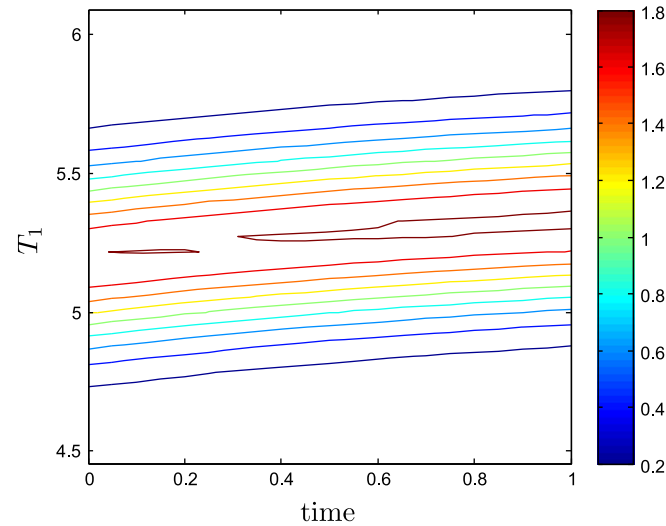


Fig. 6. Temporal evolution of CG-1A counterreceptor concentration on cell surfaces for an increased initial CG-1A concentration. The graph shows a contour plot of the frequency distribution of CG-1A counterreceptors as a function of time. Note that the Gaussian distribution gets slightly narrower as time progresses, and the mean increases roughly linearly with time, illustrating in greater detail what can also be seen also in the bottom right graph of Fig. 5. The parameters used were $r_0 = 0.04, \delta_2 = 1, \tilde{r}_2 = 1, \tilde{c}_1 = 5, f = 0.8, d_R = 0.04, \tilde{x}_8 = 1, \tilde{v} = 0.8, \tilde{\mu} = 2, \tilde{\alpha}_K = 15$, with a logistic term (2.5) with $R_m = 6$ in the adhesion flux instead of a linear term, and the initial value of c_1^f was increased to 150% of its equilibrium value \tilde{c}_1^f .

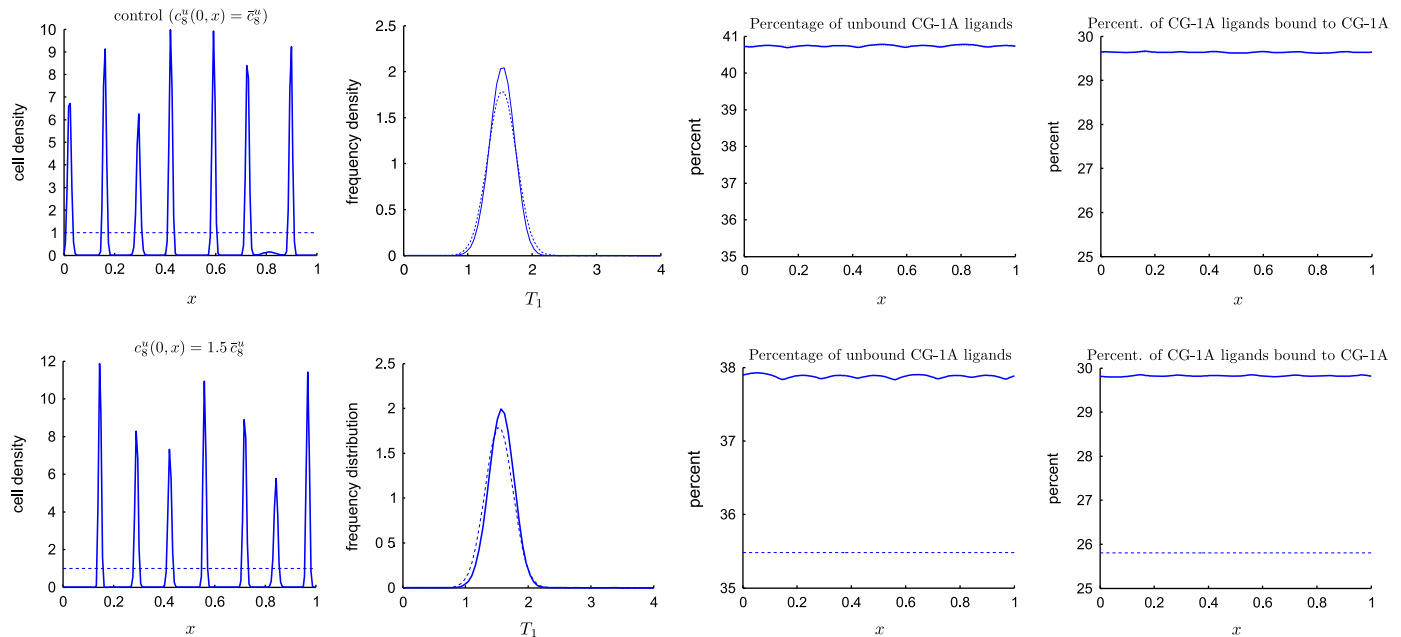


Fig. 7. Illustration of the effect of postulating an increased initial CG-8 concentration, here for the case that the percentage of unbound CG-1A counterreceptors is “large”. The first row shows plots for a simulation representing the “control” case; the second row represents the case where the initial CG-8 concentration was elevated. First column: plots of the cell density $\iint R(t, x, T_1, T_8) dT_1 dT_8$ at times $t=0$ and $t=1$ for different initial values of the freely diffusible CG-8 concentration $c_8^f(t, x)$. In all graphs, initial distributions ($t=0$) are dashed, distributions at $t=1$ are solid. (Top row: “control” case; bottom row: initial CG-8 is 50% higher than the equilibrium concentration.) Second column: frequency distribution for T_1 , the CG-1A counterreceptor molecules on cell membranes, averaged over space. Third column: unbound CG-1A counterreceptors as a percentage of all CG-1A counterreceptors, plotted against space. Fourth column: CG-1A counterreceptors bound to CG-1A as a percentage of all CG-1A counterreceptors. Parameter values were as in Fig. 5. The figure illustrates that for this parameter set, increasing the initial CG-8 concentration does not change the wavenumber, i.e., the number of condensations tends to be the same as the control case. Note that initially, the percentage of CG-1A counterreceptors bound to CG-1A molecules is below that of the “control” case. However, at the end ($t=1$), it is effectively back to the level of the control case. Also note that the average total number of CG-1A counterreceptors increases slightly (second column).

We conducted numerical experiments to investigate the problem. Results are shown in Figs. 7 and 8. In the data set for Fig. 7, increasing CG-8 has no effect on the number of condensations. However, in the data set for Fig. 8, increasing CG-8 does decrease the number of condensations. What is the difference? A crucial point appears to be the percentage of CG-1A counterreceptors which are unbound.

In Fig. 7, the percentage of CG-1A counterreceptors which are unbound is relatively high (roughly 40%). For increased CG-8 (second row), the percentage of CG-1A counterreceptors bound to CG-1A is lower than the control case initially, but quickly recovers. Additionally, the average number of CG-1A counterreceptors increases slightly compared to the control case. Intuitively, what appears to happen is that the additional CG-8 molecules primarily attach to CG-1A counterreceptors which were unbound before. Thus the number of CG-1A counterreceptors bound to CG-1A, and thus the strength of cell–cell adhesion, remained relatively constant, leading to little change compared to the control case.

In contrast, in Fig. 8, the percentage of CG-1A counterreceptors which are unbound is relatively low (roughly 12%). For increased initial CG-8, the percentage of CG-1A counterreceptors bound to CG-1A is low at first and increases with time, but it remains lower than the control case by about 2 percentage points even at the end (time $t=1$). There is little change in the average number of CG-1A counterreceptors compared to the control case. Intuitively, this may be explained by the additional CG-8 molecules attaching to shared counterreceptors which were bound to CG-1A before. This affects cell–cell adhesion, ultimately leading to fewer condensations.

We also investigated the importance of other features of parameter space. One important parameter is the dimensionless number f as given in Table 4 by

$$f = \frac{\bar{\beta}_{1,1} \bar{\beta}_{8,2}}{\bar{\beta}_{1,2} \bar{\beta}_{8,1}}$$

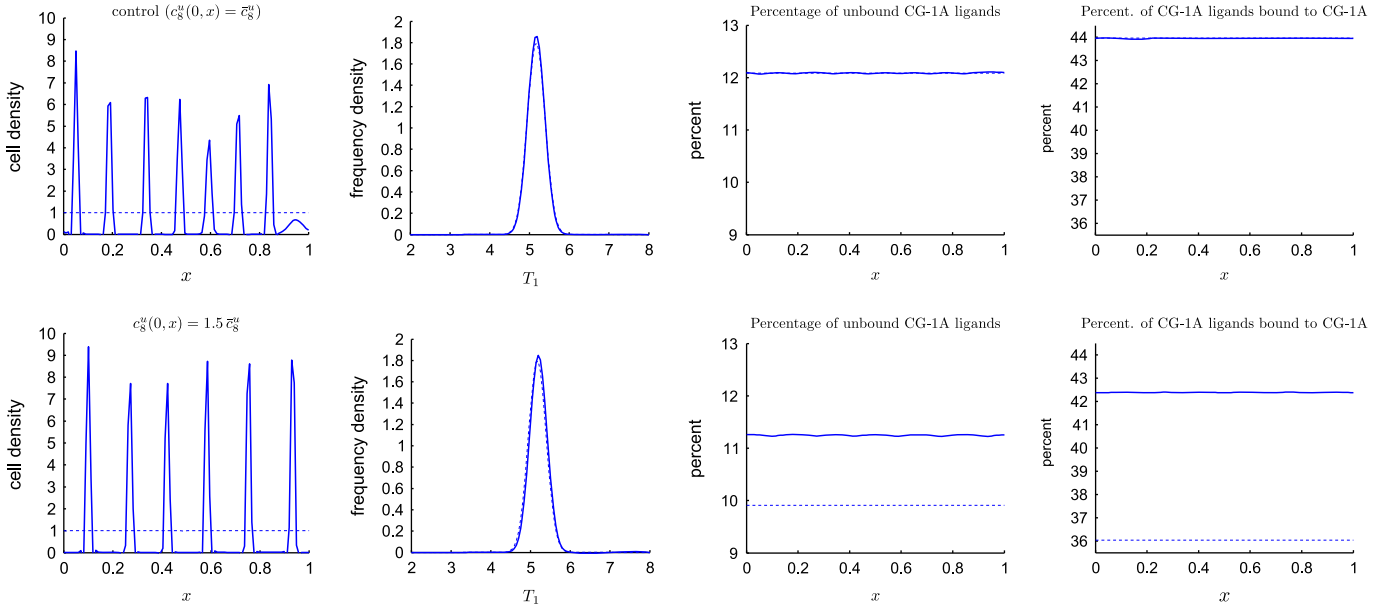


Fig. 8. An illustration of the effect of postulating an increased initial CG-8 concentration, here for the case that the percentage of unbound CG-1A counterreceptors is “small”. The graphical presentation is analogous to Fig. 7. First column: plots of the cell density $\iint R(t, x, T_1, T_8) dT_1 dT_8$ at times $t=0$ and $t=1$ for different initial values of the freely diffusible CG-8 concentration $c_8^g(t, x)$. (Top row: “control” case; bottom row: initial CG-8 is 50% higher than the equilibrium concentration.) Second column: frequency distribution of the CG-1A counterreceptor molecules on cell membranes. Third column: unbound CG-1A counterreceptors as a percentage of all CG-1A counterreceptors, plotted against space. Fourth column: CG-1A counterreceptors bound to CG-1A as a percentage of all CG-1A counterreceptors. Parameter values were as follows: $r_0 = 0.04, \delta_2 = 1, \tilde{\gamma}_2 = 1, \tilde{c}_1 = 5, f = 0.8, d_R = 0.04, \tilde{x}_8 = 1, \tilde{\nu} = 0.8, \tilde{\mu} = 2, \tilde{\alpha}_K = 15$. The figure illustrates that for this parameter set, increasing the initial CG-8 concentration decreases the wavenumber of the resulting cell distribution. Note that the percentage of CG-1A counterreceptors bound to CG-1A molecules remains below that in the “control” case (see rightmost column). Also note that the average total number of CG-1A counterreceptors barely increases compared to the control case. In repeated simulations, the mean number of peaks was 7.50 in the control case and 6.25 in the case of increased CG-8 ($n=4$).

Here $\bar{\beta}_{1,1}$ is the rate at which CG-8 binds to CG-1A counterreceptor and $\bar{\beta}_{1,2}$ is the rate at which CG-8 detaches from CG-1A counterreceptor. Similarly, $\bar{\beta}_{8,1}$ is the rate at which CG-8 binds to its own counterreceptor and $\beta_{8,2}$ is the rate at which CG-8 detaches from its own counterreceptor (see Table 2). So f essentially describes the relative affinity of CG-8 binding to CG-1A counterreceptor versus binding to its own counterreceptor. The value of f is not known, but one expects $f < 1$ since CG-8 should bind to its own counterreceptor more readily than to the shared counterreceptor.

To investigate the role of f , we conducted tests with the same data set as in Fig. 8 (where $f=0.8$), but with different values of f . The results are summarized in Table 5. The results suggest that increasing the initial concentration of CG-8 results in a decrease of the number of condensations compared to the control case only for the values $f=0.8$ and $f=0.6$. For $f=0.4$ and $f=0.2$, the number of condensations does not change significantly. These results strongly suggest that a decrease in the number of condensations for increased initial CG-8 concentrations only occurs if f is above a certain threshold, which in this case lies somewhere between $f=0.4$ and $f=0.6$. (The percentage of unbound CG-1A counterreceptors increases as f decreases, so the observed behavior is also consistent with the previously observed importance of this percentage as described above. However, the increase is relatively small.)

4.2.5. Logistic dependence on cell adhesion flux and galectin patterns

In the simulations of the previous sections, we used the linear form (2.4) in the adhesion flux $RK(R)$ given by (3.16). We now briefly discuss the case of the logistic form as in (3.18):

$$\tilde{\sigma}(R) = \frac{\tilde{R}_m}{\tilde{R}_m - \tilde{R}} R \max\left(1 - \frac{1}{\tilde{R}_m} \int_0^\infty \int_0^\infty R dT_1 dT_8, 0\right)$$

Here we used $\hat{\tilde{R}} = 1$. As discussed in the text after (2.5), this logistic form takes into account that above a certain threshold cell density,

the attractive flux due to adhesion is effectively balanced by a repellent flux due to volume exclusion effects (Armstrong et al., 2006).

To see how this changes the simulation results, consider Fig. 9. This uses the same parameters as Fig. 8, but with a logistic term (2.5) with $R_m = 12$ in the adhesion flux instead of a linear term.

A comparison of Fig. 9 (central row) with Fig. 8 shows that the logistic term leads to less dense peaks and denser valleys between peaks, but otherwise there is little qualitative difference in the profiles. See also the discussion by Armstrong et al. (2006).

These figures also illustrate that the model predicts a spatial pattern in the distribution of bound galectins: within condensations, there are more bound galectins, even if the galectin concentration is normalized by cell density³. This result agrees with experimental findings of Bhat et al. (2011), where an important result was that the higher concentrations of galectins in chondrogenic condensations were not an artifact of the higher cell density in condensations, but rather that both galectins were preferentially elevated on a per cell basis at the sites of condensation. See also the discussion in the Introduction (Section 2.1) and more analysis of this point in Section 4.3.

4.3. Exploration of the instability mechanism

In previous sections, we showed that the model can reproduce some key experimental results, and that it can be used to make some predictions for new experiments. We note that when building the model, we did not explicitly implement a mechanism for pattern formation, but we modeled what we considered to be key features of

³ A logistic or other nonlinear flux term is required for this analysis. This is because a linear term leads to very dense condensation peaks and regions with very low density between peaks (Fig. 5), which makes normalizing by the cell density numerically problematic.

Table 5

Role of the parameter f . The data was the same as that used in Fig. 8, except that the value of f was changed to the values shown below. The values below are averages of several simulations.

f	# Peaks (control: $c_8^u(0, x) = \bar{c}_8^u$)	# Peaks ($c_8^u(0, x) = 1.5 \bar{c}_8^u$)	% unbound CG-1A counterreceptors
0.8	7.5	6.25	12.0
0.6	8.3	6.3	13.6
0.4	7.50	7.75	15.5
0.2	8.0	8.0	18.0

the system. Thus while the simulations described in the previous section gave some indications of the nature of the mechanism for pattern formation, the focus was on verifying that the system has pattern forming capabilities rather than investigating the mechanism.

In this section, we investigate the nature of the pattern formation mechanism; that is, we address the problem *how* the model can give rise to cellular patterns.

For this, an analytical investigation using the standard technique of linearization would be useful. Unfortunately, the behavior equations (3.9)–(3.11) are hard to investigate analytically at the formal steady state (found in Appendix B) as the morphogenetic density is of the form $R(T_1, T_8) = R_0 \delta(T_1 - \bar{T}_1) \delta(T_8 - \bar{T}_8)$, where $\delta(x)$ denotes the Dirac distribution. Since this is not a strong solution, standard techniques for investigating stability by linearization do not apply.

To address these problems, we consider what we call the “reduced system”. This system is obtained by the additional assumption of “fast counterreceptor expression” (see below for more details). This assumption is a simplification, and indeed with this model, certain experimentally observable effects cannot be reproduced, such as the fact that with added CG-8, the number of condensations is reduced. However, the behavior of this reduced model in the control case is quite similar, and the reduced model has the advantage that it is readily analyzable by means of a standard linear stability method, which provides insight about the nature of the pattern-forming instability.

We first derive this reduced model in the next section and then investigate it analytically. The results of this analysis are then used to elucidate the mechanism of pattern formation in the model, which we address in the next subsection.

4.3.1. Reduced model

The system (3.9)–(3.11) can be greatly simplified under the assumption that counterreceptor production is fast compared to production of galectins. This assumption may be justified by the smaller number of molecules required to populate the cell surface compared to that necessary to produce a critical concentration of extracellular proteins like CG-1A and CG-8. Nonetheless, there are no data that bear on this supposition and we have not used it in the investigation of the “full system” of Eqs. (3.9)–(3.11) in Section 4.2. However, the simplified equations can provide some insights into the behavior of the full system, and they are easier to analyze analytically and numerically. In the “control” case, when initial conditions are chosen as the steady state with a small random perturbation, the reduced system (4.2)–(4.4) gives qualitatively similar results to the “full system” (3.9)–(3.11) (see Fig. 11).

The assumption of fast counterreceptor production yields an equation for $R(t, x, T_1, T_8)$ of the form:

$$R(t, x, T_1, T_8) = R(t, x) \delta(T_1 - \bar{T}_1) \delta(T_8 - \bar{T}_8) \quad \text{with}$$

$$\bar{T}_1 = \bar{T}_1(c_1^u, c_8^u), \quad \bar{T}_8 = \bar{T}_8(c_1^u, c_8^u).$$

where \bar{T}_1 and \bar{T}_8 are the formal steady state total counterreceptor concentrations. These values \bar{T}_1 and \bar{T}_8 can be found via the equations:

$$\tilde{\gamma}(c_1^u, c_8^u, T_1) = 0, \quad \tilde{\delta}(c_8^u, T_8) = 0,$$

with the functions given in (3.14) and (3.15), respectively. This yields

$$\bar{T}_1 = (1 + c_1^u + f c_8^u) \frac{2c_1^u - \tilde{\gamma}_2 \tilde{c}_1}{\tilde{\gamma}_2 c_1^u}, \quad \bar{T}_8 = \frac{1 + c_8^u}{\tilde{\delta}_2}$$

We consider the case with a logistic term in the cell adhesion flux as in (2.5). Using this in the system (3.9)–(3.11) gives the following simplified system for $R(t, x)$, $c_1^u(t, x)$ and $c_8^u(t, x)$ which we refer to as the “reduced system”:

$$\frac{\partial R}{\partial t} = d_R \nabla^2 R - \nabla \cdot (\mathbf{R}\mathbf{K}(R)) \quad (4.2)$$

$$\frac{\partial c_1^u}{\partial t} = \nabla^2 c_1^u + \frac{\tilde{\nu}}{\delta_2} R c_8^u - c_1^u \quad (4.3)$$

$$\frac{\partial c_8^u}{\partial t} = \nabla^2 c_8^u + \frac{\tilde{\mu}}{\tilde{\gamma}_2} (2c_1^u - \tilde{\gamma}_2 \tilde{c}_1) R - \tilde{\pi}_8 c_8^u. \quad (4.4)$$

Here $\mathbf{K}(R)$ can be specified using (3.16). This gives (in one spatial dimension)

$$\mathbf{K}(R(t, x)) = \tilde{\alpha}_K \frac{2c_1^u(t, x) - \tilde{\gamma}_2 \tilde{c}_1}{\tilde{\gamma}_2} \int_{-r_0}^{r_0} \tilde{\sigma}(R(t, x+s)) \frac{2c_1^u(t, x+s) - \tilde{\gamma}_2 \tilde{c}_1}{\tilde{\gamma}_2} \frac{s}{|s|} ds,$$

where we now used a logistic dependence of the flux on the morphogenetic density as in (3.18).

4.3.2. Linear stability analysis of the “reduced system”

The reduced system (4.2)–(4.4) has the steady state:

$$\bar{R} = 1, \quad \bar{c}_1^u = \frac{\tilde{\mu} \tilde{\nu} \tilde{c}_1 \tilde{\gamma}_2}{2\tilde{\mu} \tilde{\nu} - \tilde{\gamma}_2 \tilde{\delta}_2 \tilde{\pi}_8}, \quad \bar{c}_8^u = \frac{\tilde{\delta}_2}{\tilde{\nu}} \bar{c}_1^u.$$

In a standard steady state linear stability analysis (in one spatial dimension), consider first order solutions of the form:

$$R(t, x) = \bar{R} + \delta R e^{ikx + \lambda t}, \quad c_1^u(t, x) = \bar{c}_1^u + \delta c_1^u e^{ikx + \lambda t}, \\ c_8^u(t, x) = \bar{c}_8^u + \delta c_8^u e^{ikx + \lambda t}.$$

This gives the dispersion relation for the wavenumber k and growth rate λ as

$$A(k) \begin{pmatrix} \delta R \\ \delta c_1^u \\ \delta c_8^u \end{pmatrix} = \lambda \begin{pmatrix} \delta R \\ \delta c_1^u \\ \delta c_8^u \end{pmatrix}, \quad (4.5)$$

with the linearization matrix $A(k)$ given by

$$A(k) = \begin{pmatrix} a_{11}(k) & a_{12}(k) & 0 \\ \tilde{\nu} \frac{1}{\delta_2} \bar{c}_8^u & -k^2 - 1 & \frac{\tilde{\nu}}{\delta_2} \\ \tilde{\mu} \left(2 \frac{\bar{c}_1^u}{\tilde{\gamma}_2} - \bar{c}_1 \right) & 2 \frac{\tilde{\mu}}{\tilde{\gamma}_2} & -k^2 - \tilde{\pi}_8 \end{pmatrix}$$

Here we used

$$a_{11}(k) = -k^2 d_R - 2\tilde{\alpha}_K \frac{R_m - 2}{R_m - 1} \left(2\bar{c}_1^u - \tilde{\gamma}_2 \frac{\tilde{c}_1}{\tilde{\gamma}_2} \right)^2 (\cos(r_0 k) - 1),$$

$$a_{12}(k) = -4 \frac{\tilde{\alpha}_K}{\tilde{\gamma}_2} \left(2\bar{c}_1^u - \tilde{\gamma}_2 \frac{\tilde{c}_1}{\tilde{\gamma}_2} \right) (\cos(r_0 k) - 1).$$

4.3.3. Pattern-forming instability

A steady state pattern can form if for some wavenumber k , a corresponding temporal eigenvalue λ as determined by the dispersion relation (4.5) is real and positive. As an example, we consider the reduced system corresponding to the parameter set used in Fig. 8. Fig. 10 (left panel) shows the corresponding plot of the maximum temporal eigenvalue σ versus the wavenumber k as obtained from the dispersion relation (4.5). One sees that there is a

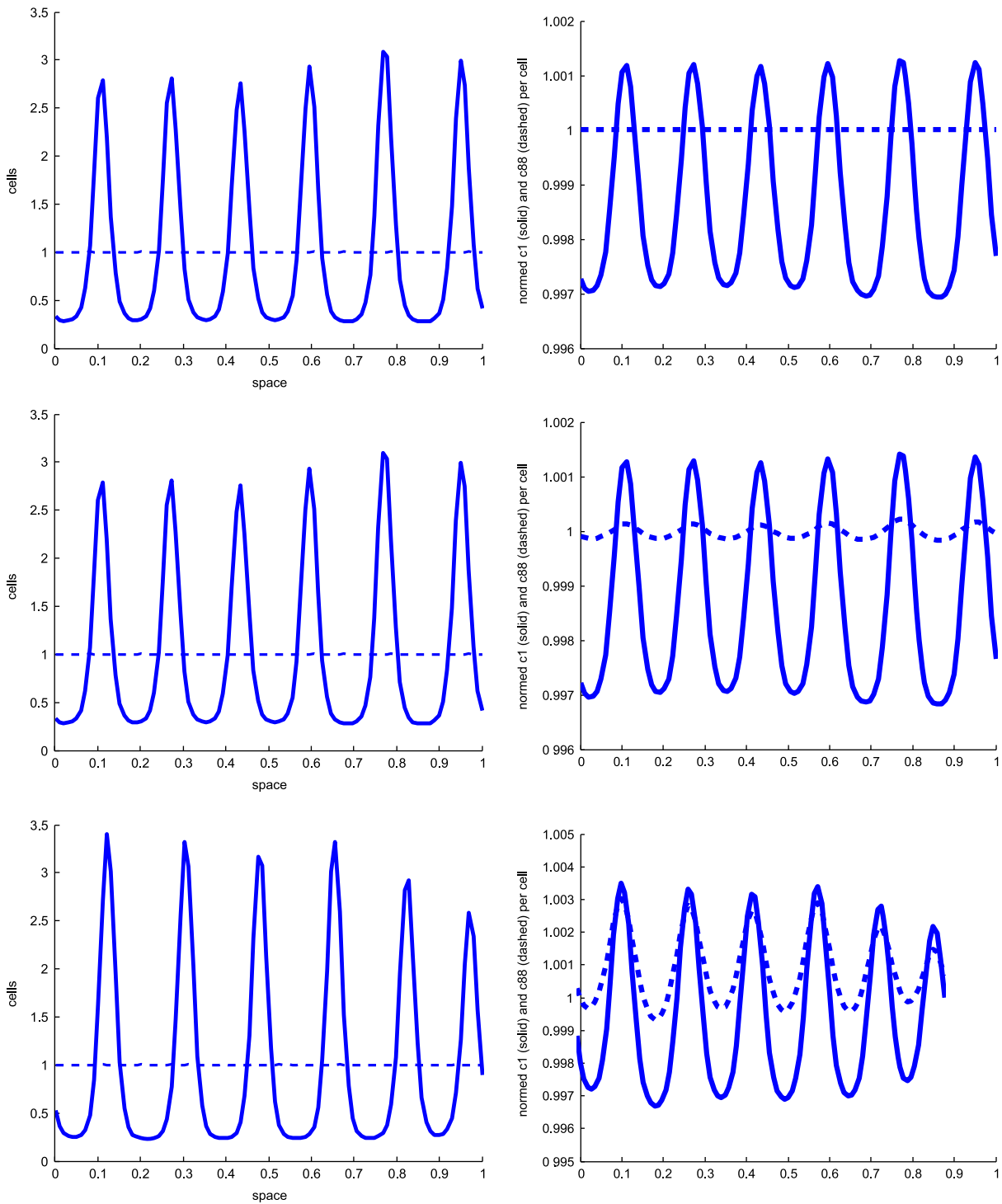


Fig. 9. Comparison of several simulations with logistic term in the cell adhesion flux and different values of galectin diffusion coefficients. The same parameter set as in Fig. 8 was used, but with a logistic term (2.5) with $R_m=7$ in the adhesion flux instead of a linear term. (The same parameter set was used for Fig. 6.) *Left column:* cell density as a function of space. *Right column:* spatial distribution of CG-1A bound to its counterreceptor (solid line) and CG-8 bound to its counterreceptor (dashed line), both at time $t=1$. The scale is chosen so that the initial distribution corresponds to the value 1. Note the relatively low amplitude of the patterns. Top row: diffusible galectin concentrations are kept constant (in time and space) at the equilibrium levels, corresponding to effectively infinite diffusion of unbound galectins. Note that the concentration of bound CG-8 is spatially homogeneous, but there is still a pattern in the bound CG-1A concentration. Center row: “control” case: diffusion coefficient of the galectins at the same value $d=1$ as in Fig. 8. Note that the amplitude of bound CG-1A is increased, and the spatial distribution of CG-8 now displays a spatial periodicity as well. Bottom row: Diffusion coefficient of the galectins at the value $d=0.1$. Note that the cell density distribution is qualitatively unchanged, but the amplitude of bound galectins is larger.

positive eigenvalue for wavenumbers in the approximate interval $[0, 18\pi]$. This means that patterns with corresponding wavenumbers can form spontaneously from initial conditions close to the equilibrium. The maximum of the function is between $k=12\pi$ and $k=14\pi$, and hence a pattern with six or seven peaks is the most

likely to appear, although five or eight peaks are also possible. This is consistent with numerical simulations, see the left panel in Fig. 11 for a typical outcome. (The same holds for simulations of the “full model”; a spectral analysis of the spatial cellular pattern of the “control” case in Fig. 9 (scaled galectin diffusion coefficient

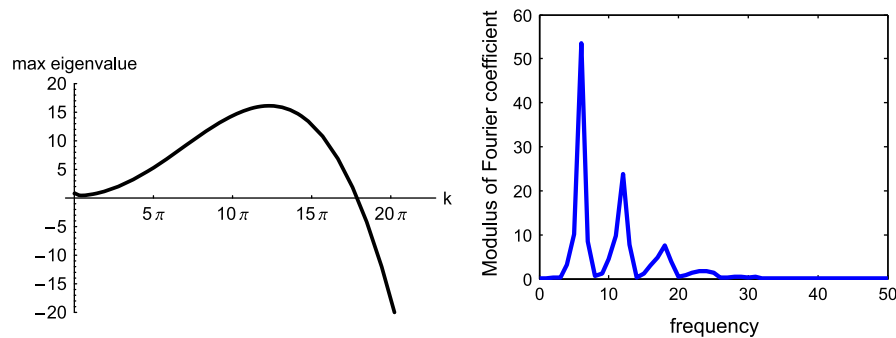


Fig. 10. *Left:* Dispersion relation for the reduced system. The parameter values were as in Fig. 8, with $R_m=3$. Plotted is the wavenumber k of the pattern versus the maximum real part of the corresponding eigenvalues (corresponding to temporal growth rate). Note that there is a maximum between $k=12\pi$ and $k=14\pi$, corresponding to patterns between five and eight maxima as the ones with largest temporal growth rates, and thus most likely to appear. Also note that at $k=0$, there is a positive eigenvalue, which corresponds to the fact that the galectin dynamics alone form a positive feedback loop. *Right:* plot of the single-sided spectrum of the amplitude of the discrete Fourier transform (DFT) of the cell density pattern shown in Fig. 9 for the “control” case (see center panel in the left column of Fig. 9; galectin diffusion coefficient $d=1$). Note the peak at $n=6$, which corresponds to a sine wave with wavenumber $k=12\pi$. Smaller peaks are at higher “harmonics” corresponding to wavenumbers $k=24\pi$ and $k=36\pi$.

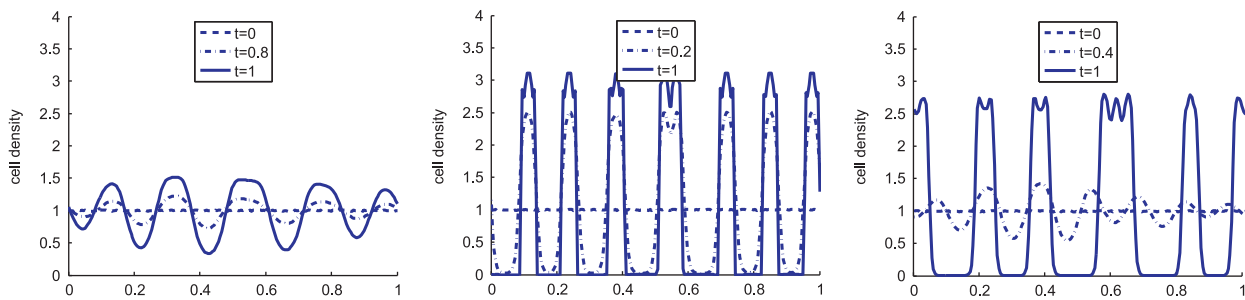


Fig. 11. Numerical simulations of the reduced system (4.2)–(4.4) for the same parameter values as in Fig. 10, with the exception of the parameters $\bar{\nu}$ and $\bar{\mu}$, which describe the rate of expression of CG-1A and CG-8, respectively (see (2.8) and (2.9) for the corresponding dimensional parameters $\bar{\nu}$ and $\bar{\mu}$, respectively). The cell density as a function of space is plotted for different times. *Left:* “control” case: $\bar{\nu}$ and $\bar{\mu}$ are as in Fig. 10. *Center:* the production rate of CG-1A, $\bar{\nu}$ is increased to $\bar{\nu}=1.6$ from the original 0.8. As described in the text, this increase in the rate at which CG-1A is produced leads to faster pattern formation, more dense condensations and a larger number of condensations. Also note that each peak is separated into fork-like smaller peaks. This is probably due to the fact that the concentration of CG-1A is increasing during condensation, so that first large condensations form, and then within each condensation, two or more “sub-condensations” form. It is not clear whether this modeling effect has any correspondence in experiments. *Right:* the production rate of CG-8, $\bar{\mu}$ is increased to $\bar{\mu}=4$ from the original 2. The pattern forms faster and the resulting condensations are denser. Note however that there is little effect on the wavenumber of the pattern (see also Section 4.3.5 for further discussion of the role of CG-8).

$d=1$; center left panel) reveals that indeed the mode corresponding to wavenumber $k=12\pi$ has by far the largest amplitude in the discrete Fourier transform, see right panel in Fig. 10.) Also note that at $k=0$, in the spatially homogeneous case, there is a small positive temporal eigenvalue. This corresponds to the fact that the galectin dynamics form a positive feedback loop.

The results of the linear stability analysis also allow for an investigation of the region in parameter space where the system can produce spatial patterns in the cell density. The gray region in Fig. 12 shows those points in $\bar{c}_1\bar{\alpha}_K$ parameter space where there is a wavenumber k with corresponding positive temporal growth rate. For instance, this plot shows that for large enough values of the adhesion strength coefficient α_K , the system can produce patterns.

4.3.4. Instability mechanism

We now seek to explain *how* the system can produce patterns, that is, we seek an intuitive understanding for its pattern formation capabilities.

As indicated above (see Section 4.2), cell–cell adhesion appears to be a crucial aspect of this mechanism. This is substantiated by a closer examination of the eigenvector at the most unstable wavenumber $k=12\pi$ in Fig. 10 (i.e., the one with the largest corresponding temporal growth rate), which reveals more about the nature of the pattern forming instability. At $k=12\pi$, the corresponding maximum eigenvalue is +16.1, and the eigenvector is $(\delta R, \delta c_1^d, \delta c_8^d) = (1, 0.003, 0.003)$. This means that the amplitude of the corresponding pattern in the cell density will be much larger

than the amplitude in the diffusible galectins. In fact, one can deduce that the pattern forming instability is primarily due to the physical interaction of the cells; the spatial pattern in the diffusible galectins seems to be of little significance in the pattern formation process. More evidence for this is supplied in Fig. 9, which shows the result of simulations of the “full” system with different values for the diffusivity of the galectins. As can be seen, even if the galectins diffuse effectively infinitely fast, spatial patterns in the cell density can form (top row). Similarly, if galectin diffusion is very low (1/10th of the original values, bottom row), patterns form. Thus it appears that the way galectins diffuse is not an important factor for pattern formation. In fact, in a similar vein, we show in Section 4.4 that under the assumption of zero cell motility, the system is incapable of forming spatial patterns in the concentrations of the galectins or their counterreceptors.

Thus the main driving mechanism behind cell condensation in the model is cell–cell adhesion, which in turn is mediated by CG-1A bound to its counterreceptor. Small differences in the initial cell density lead to the effective movement of cells toward these areas of higher concentration. Because of cell–cell adhesion, cells tend to get trapped in these protocondensations.

As cells are recruited into condensations, the immediate environments of these aggregates are depleted of cells and thereby a zone of inhibition of aggregation is created around each aggregate. The size of these depleted zones is determined by the strength of cell–cell adhesion and the effective interaction distance for cell–cell adhesion, the sensing radius ρ_0 as discussed after Eq. (2.3).

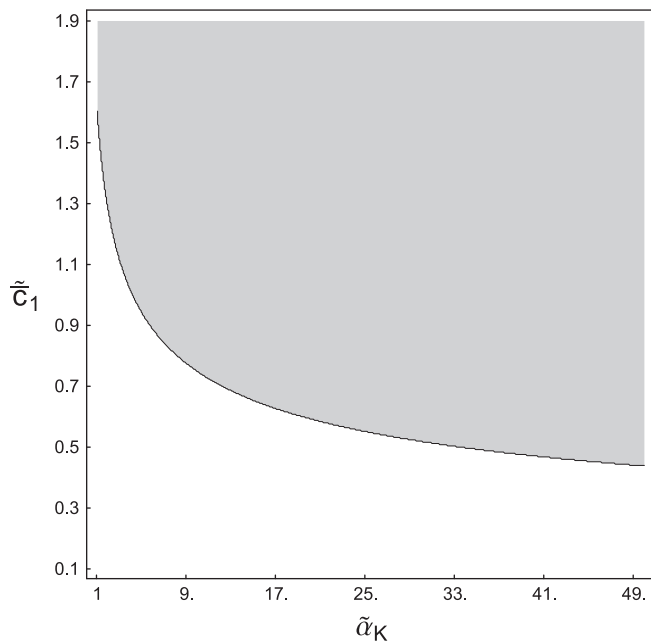


Fig. 12. Region in $\tilde{c}_1 - \tilde{\alpha}_K$ parameter space where the reduced system can produce spatial patterns. For details see the text. Other values are $r_0 = 0.04$, $\tilde{\delta}_2 = 1$, $\tilde{\gamma}_2 = 2$, $d_R = 0.04$, $\tilde{\kappa}_8 = 1$, $\tilde{\nu} = 0.8$, $\tilde{\mu} = 2$.

Thus the proposed mechanism fits into the framework of “local autoactivation–lateral inhibition” (Meinhardt and Gierer, 2000): the local autoactivation is mediated by cell–cell adhesion; cells get trapped in cell condensations and as more and more cells are recruited, there are more and more bound CG-1A molecules available for cell adhesion within these condensations. Lateral inhibition of condensation is represented by zones of depleted cell densities around each condensation.

These patterns are not always stable – for certain parameter ranges, the many small condensations eventually coalesce into one large condensation. For other parameter ranges, this does not happen, or at least not in the time frame we simulated. Here cell condensations remained separated. This is likely due to the decreased diffusion of the condensates compared to the higher diffusion of cells in the early phases of condensation; the distances between cell condensates are likely to be simply too large to allow for coalescence of condensations by diffusion alone. This is very similar to the phenomenon of partial sorting (Glazier and Graner, 1993). Both kinds of behavior are observed in experiments: while the condensations in micromass leg cultures remain separated, in wing cultures, condensations will eventually coalesce into one large cell aggregate within several days. This phenomenon appears to be connected to the fact that leg mesenchymal cells have higher cell–cell adhesion than wing mesenchymal cells (Downie and Newman, 1994, 1995; Forgacs and Newman, 2005).

There clearly is a characteristic wavelength to the patterns, as can be gleaned from Figs. 7 and 8, for instance. (A spectral analysis of the patterns using Fourier analysis confirms this, see the right panel of Fig. 10 for an example.) From the above description, it is not clear that the system should exhibit this feature. A more intuitive understanding may be obtained from the following considerations: If two condensations are sufficiently close together, cells that detach from one of the condensations can become incorporated into the other neighboring condensation instead of getting re-absorbed into the one they came from. The distance at which two condensations are “sufficiently close” so that they will coalesce, determines the wavelength of the pattern. This distance depends on the strength of cell–cell adhesion. The

stronger the adhesion, the closer the two condensations can be next to each other without coalescing, and so the smaller is the wavelength of the pattern.

Ultimately, no verbal description can make intuitive the existence of a characteristic wavelength; this can only be established with certainty by a mathematical linear stability analysis, which investigates the behavior of solutions of the sinusoidal form $\exp(ikx) = \cos(kx) + i \sin(kx)$ to the linearized equations. Indeed in the case at hand, as seen in Fig. 10, only patterns with wavelength in the interval for positive eigenvalues can form. While we stress the importance of cell–cell adhesion for pattern formation, the galectin dynamics play an important part as well. To illustrate the importance, we conducted further simulations, in which we used the same initial equilibrium concentrations as in the left panel of Fig. 11, but increased $\tilde{\nu}$, the coefficient for the rate at which CG-1A is produced in dependence of the amount of bound CG-8, to $\tilde{\nu} = 1.6$; this represents a doubling of the corresponding value for $\tilde{\nu}$. The effect is that the CG-1A/CG-8 feedback loop is activated and the amount of CG-1A is increased. This leads to more densely distributed condensations and a larger wavelength of the pattern (see center panel in Fig. 11).

The situation is more subtle if $\tilde{\mu}$ is increased, the coefficient for the rate at which CG-8 is expressed in dependence of the amount of bound CG-1A (see right panel in Fig. 11). Again, the CG-1A/CG-8 feedback loop is activated, leading to a very fast exponential growth of the concentrations of these molecules, and ultimately denser condensations, although there appears to be little effect on the wavenumber of the pattern in this case (see also Section 4.3.5 for a related discussion about simulations we conducted for the role of CG-8).

It is tempting to speculate that such simple changes in the rate of expression of one galectin in dependence of the other galectin may be instrumental in the characteristic changes in the periodicity of chondrogenic condensations in vitro corresponding to stylopod, zeugopod and autopod.

In conclusion, we can summarize our understanding of the mechanism by which patterns form in this model as follows: the feedback loop of galectin dynamics sets a characteristic concentration of CG-1A and CG-8. Spatial patterns in these concentrations have very small amplitude and generally seem to play little role. These characteristic concentrations then determine the strength of adhesion between cells. Formation of spatial patterns in the cell densities then arise through cell–cell adhesion. In these spatial patterns, cells within condensations typically have slightly higher concentrations of bound counterreceptors on their membranes, as illustrated in Fig. 9. It is possible that this slightly increased cell–cell adhesion within cell condensations lends additional stability to the periodic patterns; however, in the parameter regions we explored that this effect is relatively small.

4.3.5. The role of CG-8

In the above exploration of the pattern forming mechanism, we showed that cell–cell adhesion mediated by CG-1A plays an important role. It may be less clear what role CG-8 plays, and indeed it may seem that it is of secondary importance. To show that this is not the case, we conducted a number of computational experiments, which we briefly describe in this section. In fact, the role of CG-8 is subtle, but important. If its functionality is only slightly perturbed from the “control case” (by changing the expression rate and/or the affinity of binding to counterreceptors), the results are consistent with CG-8’s role as an effective inhibitor of condensations, that is, a combination of a lower expression rate and a lower binding rate to counterreceptors leads to more condensations (Fig. 13). However, CG-8 is also necessary for forming condensations, that is, if its functionality is completely

shut down, then no condensations form. This is due to the fact that CG-8 forms a positive feedback loop with CG-1A, and a complete “shutdown” leads to a low concentrations of CG-1A, which in turn means that cell–cell adhesion is too weak to lead to condensations.

Accordingly, our simulations in this section fall into two categories: one in which its functionality is slightly perturbed from the control case, displaying the property of CG-8 as an inhibitor of condensations in the above sense (Section 4.3.6), and one where its functionality is severely limited, leading to the inability of the system to create patterns in the spatial distribution of cells (Sections 4.3.6.1 and 4.3.6.2).

4.3.6. Perturbations of CG-8 functionality

To investigate the action of CG-8 further, we conducted a numerical study of the effect of perturbing the functionality of CG-8 on the pattern of spatial condensations. We concentrated on two parameters: the coefficient $\bar{\mu}$ for the rate at which CG-8 is expressed in dependence of the amount of bound CG-1A (see (2.9), and the counterreceptor binding coefficients $\bar{\beta}_{8,1}$ and $\bar{\beta}_{1,1}$, which describe the binding of CG-8 to the counterreceptors of CG-8 and the shared counterreceptor (i.e., CG-1A counterreceptor), respectively (see Table 2). In the non-dimensionalization we chose, this corresponds to changes in the dimensionless parameter $\tilde{\mu}$ (see Table 4) and changes in the reference concentrations for CG-8, \hat{c}_8^u , respectively (see Table 3).

Results are shown in Fig. 13. These simulations are consistent with experimental results, indicating the inhibitory effect of CG-8 on condensation numbers. Qualitatively, the combination of a low production rate of CG-8 and a low affinity of CG-8 to bind to counterreceptors results in higher condensation number. In general,

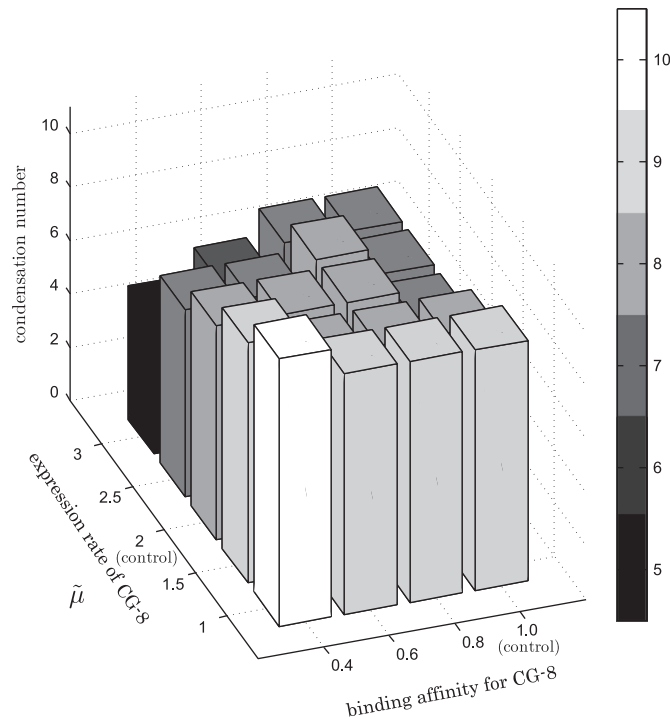


Fig. 13. Results of the simulations of condensation number following changes in the parameters governing CG-8 expression and function. Three-dimensional bar graph showing the number of condensations for several different values of two parameters: CG-1A-dependent rate of expression of CG8 (left horizontal axis) and binding affinity of CG-8 to counterreceptors (right horizontal axis). The same parameter set as in Fig. 8 was used; the values of Fig. 8 are marked as the “control” case. The graphs illustrate that CG-8 acts as an effective inhibitor of condensation numbers; in particular, a low production rate combined with a low binding affinity to counterreceptors leads to increased condensation numbers (bottom left region of the graph) (see also Fig. S3 in the Supplementary Material, where plots of the cell densities for the same data are shown).

higher production rates of CG-8 by CG-1A (parameter $\bar{\mu}$) correspond to lower condensation numbers, consistent with CG-8’s inhibitory effect on condensations. In general, changing the production rate of CG-8 alone has this effect as well, but the combined effect of both changes in the production rate of CG-8 and the binding affinity to counterreceptors simultaneously yield a stronger effect.

The effect of changing the binding rate of CG-8 to counterreceptors alone is more subtle: on the one hand, lowering the binding affinity to the shared counterreceptor (i.e., CG-1A counterreceptor) tends to decrease the competition of CG-8 for CG-1A counterreceptor and hence potentially means increased cell–cell adhesion and hence higher condensation numbers. On the other hand, the binding of CG-8 to its counterreceptor is required for the production of CG-1A, and hence lowering this binding rate leads to a decreased production of CG-1A, which can lead to decreased cell–cell adhesion and a corresponding decrease in the condensation numbers. The net effect of decreasing the CG-8 binding rate is a combination of these two opposing effects. Correspondingly, Fig. 13 does not display a straightforward relation between the counterreceptor binding rate and the condensation number (see also the discussion in Section 4.2.4).

4.3.6.1. Repressing binding to counterreceptors. While the previous section illustrated that CG-8 acts effectively as an inhibitor of condensation numbers, we also conducted several simulations to show that it is nevertheless indispensable for condensation, that is, if CG-8 functionality is completely shut down, then no condensations can form.

In the first such illustration, we simulated repressing the binding of galectins to counterreceptors. This results in the inability of cells to form condensations. (Note that the binding of CG-1A to its counterreceptors is also prevented; for simulations in which only CG-8 functionality was affected, see the next section.)

In our simulations, the galectin/counterreceptor binding coefficients $\bar{\alpha}_1$, $\bar{\beta}_{8,1}$ and $\bar{\beta}_{1,1}$ (see Table 2) were decreased to a fraction of the “control” values, decreasing drastically the rate at which galectins bind to counterreceptors. In the non-dimensionalization we chose, this corresponds to an increase in the reference concentrations \hat{c}_1^u and \hat{c}_8^u (see Table 3). We conducted numerical simulations with the same parameter set as the one used in Fig. 8, but with $\bar{\alpha}_1$, $\bar{\beta}_{8,1}$ and $\bar{\beta}_{1,1}$ decreased to 10% of their original values. Practically, this means that the non-dimensionalized initial values for c_1^u and c_8^u are decreased by 90%.

The results are shown in Fig. 14. No spatial patterns in the cell density can form. This result is easily understood by considering the cell adhesion flux term $\mathbf{K}(R)$ in (3.16): due to low initial values of c_1^u and c_8^u , the c_1^u/c_8^u interaction effectively leads to a negative feedback loop, which in turn means that c_1^u further decreases. The c_1^u -dependent term in $\mathbf{K}(R)$ is thus small, and therefore the cell–cell adhesion flux is too small to initiate formation of spatial patterns in the cell density.

We tested these model predictions with in vitro experiments in which a functional inhibitor of both CG-1A and CG-8 was added to cultures, see Section 4.3.6.3

4.3.6.2. Simulation of absence of CG-8. To demonstrate the importance of CG-8 for cell patterning, we conducted two experiments where crucial effects of CG-8 were taken out of the model.

In the first such test, we considered the Eqs. (3.9)–(3.11) again, but now set $\partial c_8^u/\partial t = 0$ instead of (3.11), set $\tilde{\nu} = 0$ in (3.10) and eliminated the derivative with respect to T_8 in (3.9). This corresponds to eliminating CG-8 from the dynamics. In in silico experiments, we used the same data and the same initial conditions as in the “control” case in Fig. 8. This system did not display

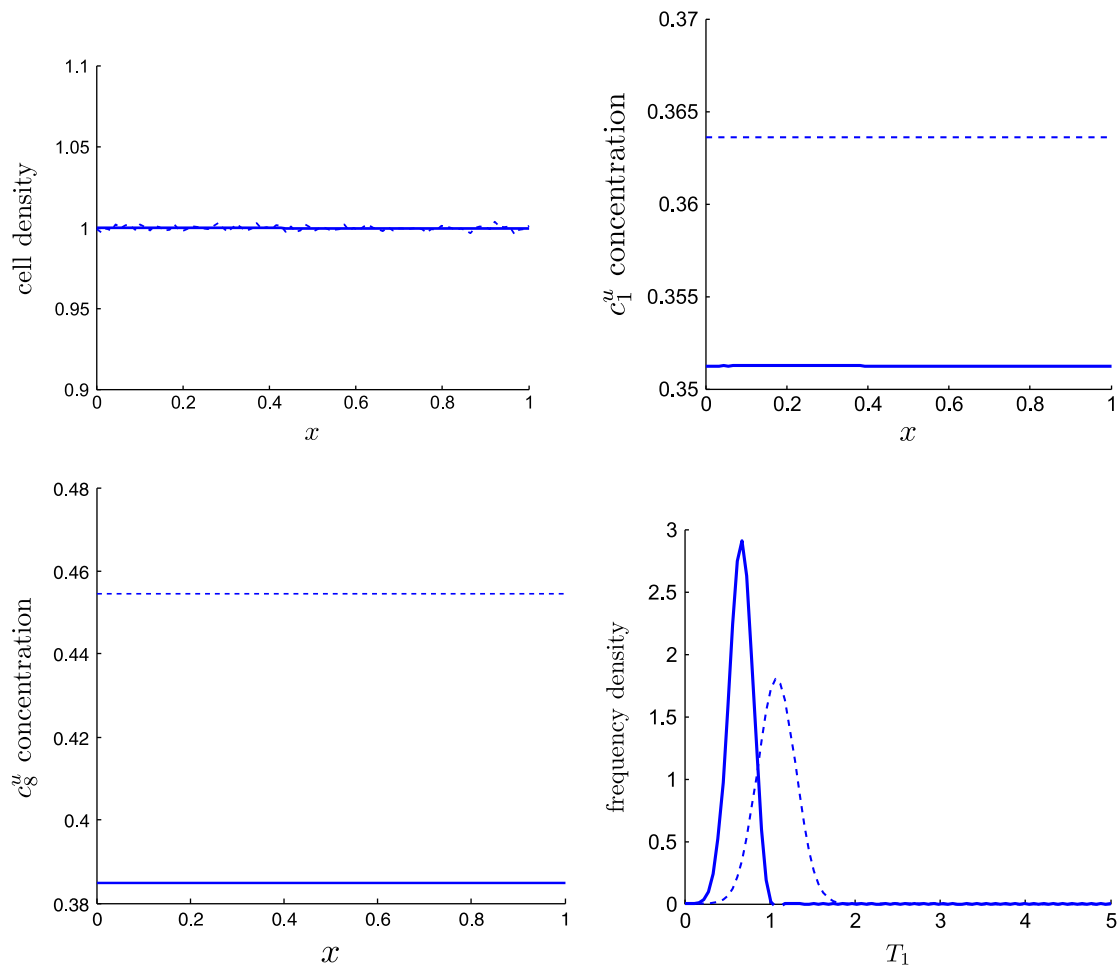


Fig. 14. Results of simulations which severely restrict binding of galectins to counterreceptors. The counterreceptor binding coefficients $\bar{\alpha}_1$, $\bar{\beta}_{8,1}$ and $\bar{\beta}_{1,1}$ (see Table 2) were decreased by 90%. The same parameter set as in Fig. 8 was used. As indicated in the text, the non-dimensionalized initial conditions for c_1^u and c_8^u are decreased by 90% compared to the control case of Fig. 8. The initial distributions for the morphogenetic density were chosen as Gaussian distributions in T_1 and T_8 as given in (4.1). The means T_1 and T_8 were chosen such that the initial values satisfy $\bar{\gamma}(\bar{c}_1^u, \bar{c}_8^u, \bar{T}_1) = 0$ and $\bar{\delta}(\bar{c}_8^u, \bar{T}_8) = 0$, so that initial production of T_1 and T_8 are in equilibrium (see (3.14) and (3.15)). Initial distributions are dashed, distributions at the final time $t=1$ are solid. The graphs illustrate that there is a breakdown of the feedback loop between the counterreceptors, which causes all concentrations to decrease, and cell–cell adhesion is insufficient to form spatial patterns. *Top left:* cell density as a function of distance. Note that no spatial patterns are displayed. *Top right:* spatial distribution of unbound CG-1A. Note that these levels decrease significantly from the initial levels. *Bottom left:* spatial distribution of unbound CG-8. Again these levels decrease significantly from the initial levels. *Bottom right:* frequency distribution of the CG-1A counterreceptor molecules on cell membranes. Note that the mean number of CG-1A counterreceptors decreases from the initial value.

spatial patterns; again the reason was that the absence of the CG-1A/CG-8 feedback loop led to a rapid decrease of c_1^u , which meant that the cell-adhesion flux $\mathbf{K}(R)$ was too low to initiate cellular patterning (results not shown).

We also conducted experiments where the action of CG-8 was restricted in a slightly less severe way, namely by setting the parameter μ to zero in (3.10). This means that CG-8's ability to initiate CG-1A synthesis is eliminated. All other terms in (3.9)–(3.11) were kept the same. Again, simulation shows that no spatial patterns in the cell density can form, because again the CG-1A/CG-8 feedback loop responsible for maintaining high levels of CG-1A was eliminated (Fig. 15).

4.3.6.3. Experimental confirmation of some simulation results.

The predictive power of the model was tested by in vitro experimental confirmation of its prediction, based on simulations, that treatment of cultures with a functional inhibitor of both CG-1A and CG-8 (e.g., lactose) would lead to breakdown in condensation formation and patterning (see Section 4.3.6.1). Freshly prepared micromass cultures were treated with serum-free defined medium alone, or supplemented with 20 mM lactose or 20 mM sucrose (a

control for steric and osmotic effects). The cultures were grown for 48 h, fixed and stained with peanut agglutinin (PNA), a condensation marker. When compared to untreated control cultures, lactose-added cultures showed lack of condensations, with no PNA patterns discernible. In contrast, sucrose-added cultures showed a condensation pattern similar to untreated cultures (Fig. 16). The results of experimental perturbation of the CG-1A–CG-8 network therefore confirm the behavior of the perturbed in silico network.

4.4. Investigation of a possible “morphostatic” mechanism

The mechanism discussed in the previous section crucially depends on cell motility and cell–cell adhesion. Emergence of patterns in the spatial distribution of galectins forms concurrently with the emergence of patterns in the cell distribution, and the two processes are interdependent. According to the classification by Salazar-Ciudad et al. (2003), such processes are called “morphodynamic”. This is qualitatively different from mechanisms which involve a chemical prepattern. In such mechanisms, a pattern in some morphogen is set up first, which then induces the cells to move toward the centers of high concentration and thus serves as the template for the cell distribution. Such chemical

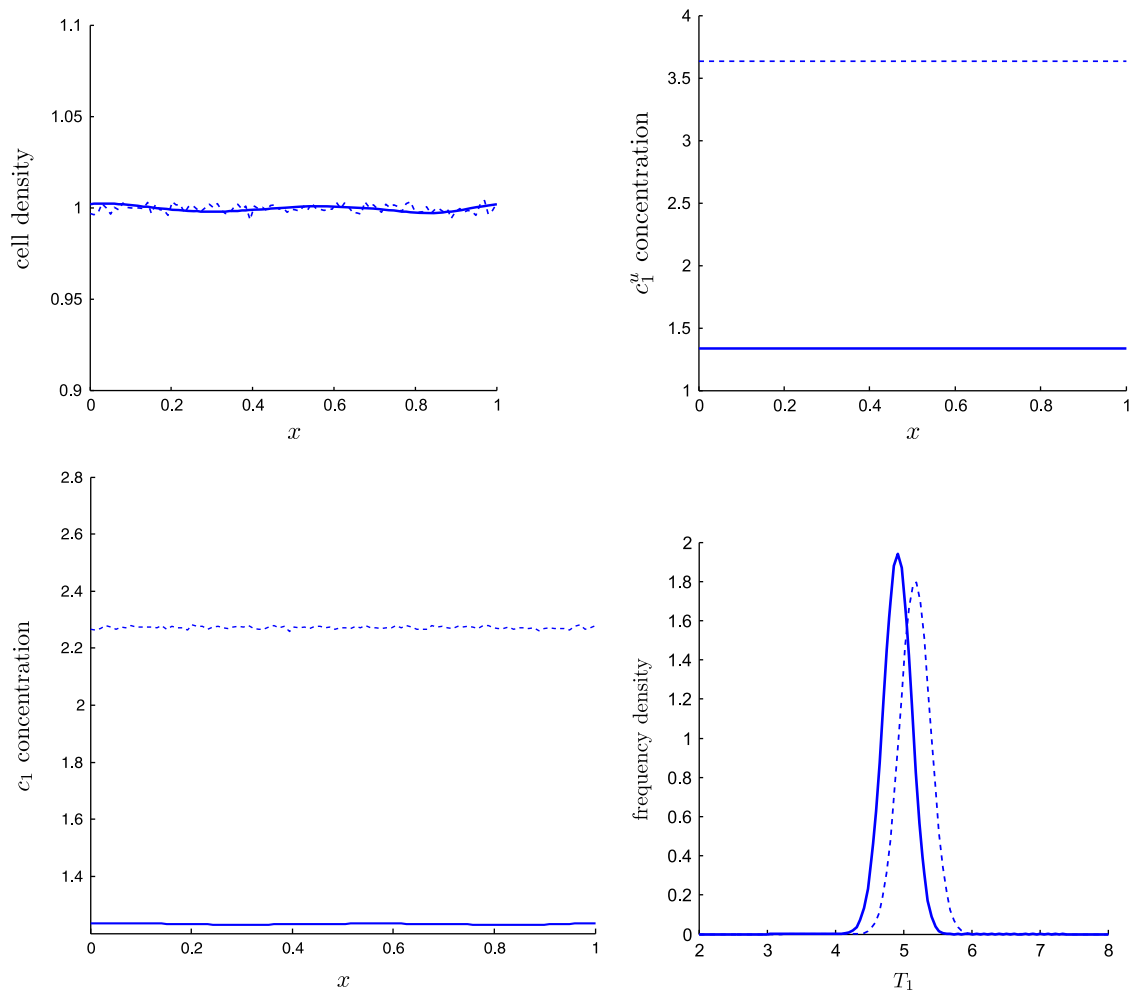


Fig. 15. Results of simulations where the effect of CG-8 on CG-1A synthesis was eliminated. The same parameter set as in Fig. 8 was used, but with $\bar{\mu} = 0$. The initial conditions were chosen as in the “control case” of Fig. 8. Initial distributions are dashed, distributions at the final time $t=1$ are solid. *Top left:* cell density as a function of distance. Note that no spatial pattern is displayed. (The final pattern has a very small amplitude, but is negligible compared to the “control” case in Fig. 8.) *Top right:* spatial distribution of unbound CG-1A. Note that due to the absence of CG-1A synthesis, these levels decrease significantly from the initial levels. *Bottom left:* spatial distribution of CG-1A bound to its counterreceptor. Again, these decrease significantly in the time frame, which in turn decreases cell–cell adhesion. *Bottom right:* distribution of CG-1A counterreceptor. Note that the average concentration of CG-1A counterreceptor also decreases during the time frame.

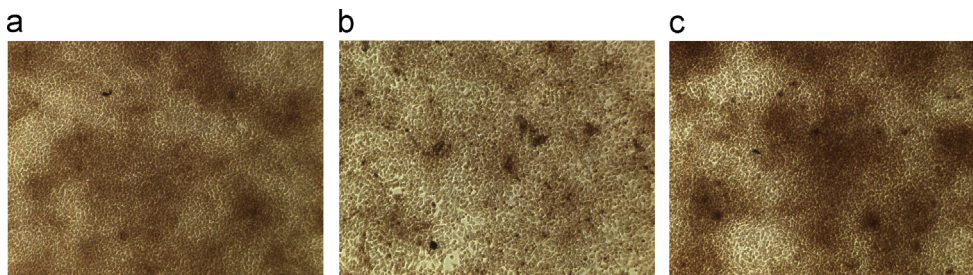


Fig. 16. Addition of galectin binding inhibitor lactose decreases condensation number and size in culture. (a) Nodular pattern of condensations marked by *Arachis hypogaea* lectin (PNA) staining of a fixed 2-day control leg culture. (b) Culture treated with 20 mM lactose shows a decrease in number of condensations with a uniform decrease in their sizes. (c) Culture treated with 20 mM sucrose (control non-specific sugar) does not show a significant change in number and size of condensations. Images (a–c) are at the same magnification and photographed with a $16\times$ objective.

prepattern mechanisms are referred to as “morphostatic” according to the classification by Salazar-Ciudad et al. (2003).

In this section, we investigate whether the original full model involving freely diffusible galectins and the morphogenetic density as given in (2.2), (2.8) and (2.9) can actually give rise to “chemical prepatterns”; that is whether it is possible for some parameter ranges to generate patterns even in the absence of any cell motility.

To do so, we first derive in Section 4.4.1 a new system of equations from Eqs. (2.2), (2.8) and (2.9) under the assumption of zero cell motility. We call this system the “core morphostatic system”. To investigate whether this system can give rise to chemical prepatterns, we set up two minimum requirements, formulated at the end of Section 4.4.2. We then argue that the “core morphostatic” system does not satisfy one of these

conditions, and thus that it is not capable of pattern formation. (We discuss additional assumptions on the regulatory galectin network that can indeed lead to patterns, and discuss the findings in the Supplementary Text S1.)

4.4.1. “Morphostatic limit” of the full galectin system

To consider the absence of cell motility, we set the cell diffusivity D_R and the adhesion strength $\bar{\alpha}_K$ both to zero in (2.2). It follows then from (2.2) that

$$\frac{\partial}{\partial t} \int R(t, \mathbf{x}, c_1, c_8^s, c_8^1, \ell_1, \ell_8) dP = 0.$$

(Here we used the notation dP as in (2.1).) Thus the cell density $R_{\text{tot}}(t, \mathbf{x}) = \int R dP$ is locally conserved, as is consistent with zero cell motility. We assume that the initial cell density satisfies $R_{\text{tot}}(0, \mathbf{x}) = R_0 = \text{const}$, so that $R_{\text{tot}}(t, \mathbf{x}) = R_0$ for all t .

We then define the concentration of CG-1A bound to the shared counterreceptor as

$$G_1(t, \mathbf{x}) = \int c_1 R dP,$$

and similarly

$$G_8^1(t, \mathbf{x}) = \int c_8^1 R dP \quad \text{CG-8 bound to the shared counterreceptor}$$

$$G_8^8(t, \mathbf{x}) = \int c_8^8 R dP \quad \text{CG-8 bound to its counterreceptor}$$

$$L_1(t, \mathbf{x}) = \int \ell_1 R dP \quad \text{shared counterreceptors, unbound}$$

$$L_8(t, \mathbf{x}) = \int \ell_8 R dP \quad \text{CG-8 counterreceptors, unbound}$$

In the following, we assume that all these quantities are finite at each spatial point and for all time. Using (2.2), (2.8) and (2.9), we can now derive a system of equations for the above concentration and the free galectin concentrations (This can be done by (formal) integration by parts from (2.2) using the boundary conditions (2.7).):

$$\frac{\partial G_1}{\partial t} = \bar{\alpha}_1 c_1^u L_1 - \bar{\alpha}_2 G_1 \tag{4.6}$$

$$\frac{\partial G_8^8}{\partial t} = \bar{\beta}_{8,1} c_8^u L_8 - \bar{\beta}_{8,2} G_8^8 \tag{4.7}$$

$$\frac{\partial G_8^1}{\partial t} = \bar{\beta}_{1,1} c_8^u L_1 - \bar{\beta}_{1,2} G_8^1 \tag{4.8}$$

$$\frac{\partial L_1}{\partial t} = \bar{\gamma}_1 G_1 - \bar{\gamma}_2 L_1 - \frac{\partial G_1}{\partial t} - \frac{\partial G_8^1}{\partial t} \tag{4.9}$$

$$\frac{\partial L_8}{\partial t} = \bar{\delta}_1 - \bar{\delta}_2 L_8 - \frac{\partial G_8^8}{\partial t} \tag{4.10}$$

$$\frac{\partial c_1^u}{\partial t} = D_1 \nabla^2 c_1^u + \bar{\nu} G_8^8 - \bar{\alpha}_1 c_1^u L_1 + \bar{\alpha}_2 G_1 - \bar{\pi}_1 c_1^u \tag{4.11}$$

$$\frac{\partial c_8^u}{\partial t} = D_8 \nabla^2 c_8^u + \bar{\mu} G_1 - \bar{\beta}_{1,1} c_8^u L_1 + \bar{\beta}_{1,2} G_8^8 - \bar{\beta}_{8,1} c_8^u L_8 + \bar{\beta}_{8,2} G_8^8 - \bar{\pi}_8 c_8^u. \tag{4.12}$$

We will assume the two galectin diffusion coefficients to be the same: $D_1 = D_8$. Above we also used $\gamma = \bar{\gamma}_1 c_1 - \bar{\gamma}_2 \ell_1$ for the production rate of CG-1A counterreceptor.

We call the above system of equations the “core morphostatic system”. In Supplementary Text S1, we find a non-dimensionalized form for these equations, see (S1.8)–(S1.14).

4.4.2. Linear stability analysis

We investigate whether the system (4.6)–(4.12) can spontaneously give rise to spatial patterns from the equilibrium concentrations with added random chemical noise. This investigation is done by a linear stability analysis. There is a unique steady state $(\bar{G}_1, \bar{G}_8^8, \bar{G}_8^1, \bar{L}_1, \bar{L}_8, \bar{c}_1^u, \bar{c}_8^u)$ of Eqs. (4.6)–(4.12). (Formulas for the non-dimensionalized version of the system (S1.8)–(S1.14) are given in (S1.16) in the Supplementary Material.)

To investigate whether the system (4.6)–(4.12) can give rise to patterns, we consider the linearization:

$$\partial_t U = DU_{xx} + AU$$

where $U = (G_1 - \bar{G}_1, G_8^8 - \bar{G}_8^8, G_8^1 - \bar{G}_8^1, L_1 - \bar{L}_1, L_8 - \bar{L}_8, c_1^u - \bar{c}_1^u, c_8^u - \bar{c}_8^u)$ describes a vector of perturbations of the relevant chemical concentrations from their steady states. The linearization matrix A and the diffusion matrix D are given explicitly in the Supplementary Material.

Consider solutions of the form $U = e^{i\mathbf{k}\mathbf{x} + st} U_0$, where \mathbf{k} is the wave-vector of the spatial pattern, s the temporal growth rate of the pattern with wavenumber \mathbf{k} and U_0 a constant vector describing the relative sizes of the amplitudes of the pattern for each molecular species. The dispersion relation then becomes

$$sU_0 = (A - k^2 D)U_0,$$

and hence $s = s(k)$ is an eigenvalue of the matrix $A - k^2 D$, where we used the notation $k^2 = |\mathbf{k}|^2$. Stationary patterns of wavenumber k can form if $s(k)$ is real and positive. We define

$$s_{\text{max}}(k^2) = \max(\text{Eigenvalues}(A - k^2 D)) \tag{4.13}$$

Hence patterns of wavenumber k can form if $s_{\text{max}}(k^2) > 0$.

We now use the linear stability analysis to address the question whether the core morphostatic system (4.6)–(4.12) is sufficient to explain basic pattern formation as found experimentally. Our starting point is that based on the experimental evidence, the system has to display at least the following “minimum” properties:

Criterion 1: The spatially homogeneous case (wavenumber $k=0$) is unstable, since the addition of CG-1A leads to a rapid upregulation of CG-8 and vice versa. So $s_{\text{max}}(0) > 0$.

Criterion 2: The function $s_{\text{max}}(k^2)$ must attain a positive maximum for some wavenumber $k > 0$. This is because a spatial pattern with a characteristic length scale forms spontaneously in experiments.

While Criterion 1 can indeed be met, we give evidence that the core morphostatic system (4.6)–(4.12) does not meet Criterion 2 for any combination of parameters (see Fig. 17 for a generic plot of the function $s_{\text{max}}(k^2)$). In fact, a numerically aided computation shows that $s_{\text{max}}(k^2)$ is a nonincreasing function of the wavenumber k^2 , see Section S1.2 of the Supplementary Text. (Thus Fig. 17 shows a generic plot of $s_{\text{max}}(k^2)$.) It follows that the system (4.6)–(4.12) does not meet Criterion 2. Thus cell motility appears to be a crucial component of the system; without it, no patterns will form.

In Section S1.3 of the Supplementary Text, we address the further problem of what additional hypothetical regulatory interactions in the galectin network can lead to a system that is capable of generating spatial patterns. The Supplementary Text also contains an additional discussion of the results of this section.

5. Summary and outlook

We set up a mathematical model of chondrogenic condensation of mesenchymal cells involving cells, two galectins (CG-1A and CG-8) and their respective counterreceptors. We incorporated the

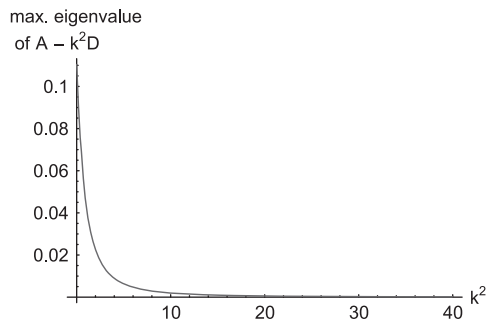


Fig. 17. Illustrative plot of $s_{\max}(k^2)$, the maximum eigenvalue of the matrix $A - k^2D$ as a function of the square of the wavenumber k^2 for the “core morphostatic” system (4.6)–(4.12). (The non-dimensionalized values of the parameters were chosen as $\pi_{C_1}^* = \pi_{C_1}^* = \pi_{C_8}^* = \pi_{I_1}^* = \pi_{I_8}^* = \pi_{C_8}^* = \pi_{C_1}^* = 1$, see Eqs. (S1.8)–(S1.14) in the Appendix.) Note that the function is decreasing monotonically, and hence no pattern with a typical wavenumber k can form spontaneously from random noise. As shown in the text, this is generically the case for the “morphostatic” system (4.6)–(4.12).

“minimum” regulatory network of galectin dynamics as sketched in Fig. 2. We showed that for a broad range of parameters, the system can spontaneously generate patterns of peaks in the cell density if started from equilibrium with small added noise. If the initial concentration of CG-1A was increased, simulating adding CG-1A to cultures, this results quite reliably in an increase in the number of peaks. If the initial concentration of CG-8 was increased, the results depended more subtly on the parameter ranges: the number of peaks was found to decrease for some parameter sets, but also to remain the same or increase in others. A determining factor was the overall percentage of unbound CG-1A counterreceptors among all CG-1A counterreceptors: If this percentage was too high, the result was no change in the number of condensations, or even an increase in the number of condensations. This behavior allowed us to make a number of experimentally testable predictions, which are listed at the end of this summary.

A combination of numerical simulations and stability analysis revealed the mechanism of pattern formation in our model. We found that the strength of cell–cell adhesion was a crucial determinant of the capability for pattern formation, and also of the wavenumber of the pattern. Small initial differences in the cell density lead to the effective movement of cells toward areas of higher concentration, where cells tend to get trapped.

These multiple condensations typically do not coalesce into one large condensation in our simulations, at least not in the time frame we simulated. This is likely due to the decreased diffusion of the condensates compared to the higher diffusion of cells in the early phases of condensation.

The strength of cell–cell adhesion in turn is determined by the number of CG-1A molecules bound to its counterreceptors on cell membranes. This consideration explains the results of the simulations when the initial amount of CG-1A was increased: this led to the formation of more complexes of CG-1A and its counterreceptor, an effect that was additionally reinforced by the fact that such complexes exert a positive control over the expression of CG-1A counterreceptor. The outcome of added CG-8 is subtler: there are two somewhat opposing effects. On the one hand, this leads to an increased production of CG-1A; on the other hand, the added CG-8 molecules may bind to shared counterreceptors which had previously been bound to CG-1A, thus competing with CG-1A molecules for available counterreceptors. The first of these effects potentially leads to an increase in cell–cell adhesivity; the second to a decrease in adhesivity. In order for the second effect to dominate, it appears to be important that the number of unbound shared counterreceptor not be too large – otherwise, the added

CG-8 will tend to bind to such unbound shared counterreceptors instead of occupying shared counterreceptors which have previously been bound to CG-1A.

We were also able to show that the model produces a spatial pattern in the distribution of CG-1A and CG-8, bound to their respective counterreceptors, which reflects the cell density. We showed that this was not an artifact of increased cell densities in condensations, but that cells within condensations actually tended to have higher concentration of such complexes of galectins with their counterreceptors (see Fig. 9). These patterns are not due to a corresponding pattern in the ECM-bound galectins; in fact, there tended to be no such spatial pattern in these concentrations. Even if the diffusivity of galectins in the ECM was assumed to be effectively infinite, a pattern in the complexes of CG-1A bound to its counterreceptor appeared, albeit no such pattern appeared in the complexes of CG-8 bound to its counterreceptor, see again the top row of Fig. 9.

The mechanism of the appearance of such spatial patterns in membrane-bound CG-1A and CG-8 appears to be as follows: in the initial aggregation process, cells that have comparably many CG-1A molecules bound on their membranes and are thus “stickier” than other cells, tend to get more easily trapped within condensations and are thus preferably found within the aggregates. Moreover, the positive control of CG-1A over its counterreceptor means that more CG-1A will be produced and bound to counterreceptors within condensations. This is additionally reinforced by the feedback of CG-1A and CG-8, which is “turned on” within condensations. Correspondingly, the smaller the diffusion coefficients of galectins, the more pronounced are the spatial galectin patterns (see again Fig. 9).

We finally treated the question of whether spatial pattern formation was also possible with zero cell motility, that is, whether the galectin network alone can generate spatial patterns. Through a linear stability analysis, we argued that this is not possible for any parameter set. With certain additional hypothesis, we found that such pattern formation capabilities could be established, but the assumptions we had to make were quite implausible from a molecular point of view.

Our main objective was the analysis of the biological processes, and a mathematically completely exhaustive treatment is beyond the scope of this paper. For instance, we implicitly assumed the existence and uniqueness of solutions to our model equations, and the positivity of solutions (as proved for the later-acting TGF- β -inhibitor–fibronectin network in the developing limb, Alber et al., 2005.) We also used an ad hoc approach to weak solutions (in this case, involving Dirac measures) without explicitly formulating a weak version of our equations or stating the corresponding function spaces for solutions. We plan to perform these analyses in a future publication.

On the modeling side, we did not aim for quantitatively realistic simulation results; given the large number of unknown parameters (such as expression rates of various proteins, or adhesion strength parameters), our goal was rather a qualitative and comparative analysis and this was reflected in the model’s prediction of the behavior of the system. Finally, it should be noted that while many of the modeling components (such as diffusion and protein secretion) are quite standard, the important modeling of cell–cell adhesion is somewhat less standard and there is currently still some debate about how to incorporate cell–cell adhesion into continuous models. (Modeling cell–cell adhesion in discrete models is arguably much better understood; see for instance, the Cellular Potts Model; Glazier and Graner, 1993.) Here we followed the approach of Armstrong et al. (2006), who modeled cell–cell adhesion via an effective adhesion flux term. This leads to nonlocal equations, i.e., dynamics involving an integral over relevant quantities. Other approaches exist, for instance by Anguige and Schmeiser (2009), who derived an equation from the continuous

limit of a model involving a biased random walk on a discrete lattice (see also Alber et al., 2006, 2007). However, we showed that the results do not qualitatively change when using different functional forms of cell–cell adhesion (linear or logistic expressions), and we expect in general that the results are largely independent of the details of specific cell–cell adhesion modeling components.

Concerning the biological implications of this work, the described pattern forming mechanism is unusual in being inherently morphodynamic in that its developmental outcomes depend on signaling and cell rearrangement being exerted in a simultaneous fashion. It shares this property with the mechanism for tooth crown patterning described by Salazar-Ciudad and Jernvall (2010). For the present case, the requirement for adhesion-driven cell movement to form any nonuniform pattern at all in the multiscale two-galectin network was unclear apart from the mathematical–computational analysis presented here, highlighting the usefulness of such analysis in disclosing non-intuitive implications of experimental results. In addition, the experimental result shown in Fig. 16 confirmed a specific prediction of this model that would not necessarily be indicated by other dynamical interpretations.

Tests of the model in the future can focus on a number of its further predictions:

1. A crucial condition for the effectiveness of adding CG-8 to antagonize condensations is that the percentage of unbound CG-1A counterreceptors among all of CG-1A counterreceptors be small. If this percentage can be increased, e.g., by over-expression of an eventually characterized counterreceptor of CG-1A, we predict that the effectiveness of CG-8 as an antagonist of condensations will decrease.
2. In a similar vein, we predict that if the affinity of CG-8 binding to its shared counterreceptor with CG-1A (as opposed to binding to its unique counterreceptor) can be decreased, the effectiveness of CG-8 as an antagonist of condensations will decrease. (In terms of the model, this corresponds to decreasing the dimensionless parameter f , see the discussion in Section 4.2.4 and also Table 5.)
3. In the model, no cellular patterns can form in the absence of cell–cell motility. Thus an immediate prediction is that decreasing cell motility in cultures will decrease the number and density of the precartilaginous condensations, and not simply attenuate the degree of cell packing at an otherwise unperturbed set of sites.
4. According to Sheth et al. (2012), the effects on the digit pattern in the mouse of the levels of Hoxa13 and Hoxd11–13 gene products are exerted through the parameters of a Turing-type reaction–diffusion mechanism underlying this process. The model presented here represents such a pattern generating reaction–diffusion system, which though pertaining specifically to the avian system, has a firmer experimental and molecular basis than any yet available for mammalian embryos. The basic similarities in Hox gene action in limb development across the amniotes suggest that certain of the parameters in (3.5)–(3.7) would be suitable loci for the computational investigation of the specific roles of the various Hox genes.

Appendix A. Convergence to Dirac measure

We consider here a simplified version of the conservation law for the morphogenetic density (2.2) and show that solutions converge to a Dirac (point) measure. Consider the equation for $R(t, T)$ given by

$$\frac{\partial R}{\partial t} = -\frac{\partial}{\partial T}(\alpha(T)R), \tag{A.1}$$

with

$$\alpha(T) = a - bT \tag{A.2}$$

for constants $a, b > 0$. Note that $\alpha(T)$ has the unique root $T_0 = a/b$. The initial condition is

$$R(t = 0, T) = R_0(T)$$

for $0 \leq T < \infty$. We assume that R_0 is nonnegative and C^1 on $(0, \infty)$ and that we can extend it to a C^1 -function on $(-\infty, \infty)$ by setting $R_0(T) = 0$ for $T \leq 0$. We also assume that

$$\int_{-\infty}^{\infty} R_0(T) dT = 1.$$

Using the method of characteristics, one obtains the following explicit expression for the solution of (A.1) with boundary condition $R(t, T = 0) = 0$:

$$R(t, T) = R_0\left(\frac{a}{b} + \left(T - \frac{a}{b}\right)e^{bt}\right)e^{bt}.$$

We now show that

$$R(t, T) dT \rightarrow \delta_{T-(a/b)} \quad \text{as } t \rightarrow \infty$$

in the sense of weak convergence of measures (Billingsley, 1999). Here $R(t, T) dT$ denotes the time-dependent absolutely continuous (with respect to the Lebesgue measure) measure on $[0, \infty)$ induced by $R(t, T)$, and $\delta_{T-(a/b)}$ denotes the Dirac (point) measure on $[0, \infty)$ supported at $T = a/b$. That is, for any Borel set $I \subseteq [0, \infty)$, we have $\delta_{T-(a/b)}(I) = 1$ if $a/b \in I$ and $\delta_{T-(a/b)}(I) = 0$ if $a/b \notin I$.

Indeed, let $\psi \in C([0, \infty))$ be a bounded continuous function. Extend it to all of \mathbb{R} by setting $\psi(T) = 0$ for $T < 0$. We then have

$$\begin{aligned} \int_0^{\infty} \psi(T)R(t, T) dT &= \int_{-\infty}^{\infty} \psi(T)R(t, T) dT \\ &= \int_{-\infty}^{\infty} \psi\left(e^{-bt}S + \frac{a}{b}\right)R_0\left(\frac{a}{b} + S\right)dS \rightarrow \psi\left(\frac{a}{b}\right) \quad (t \rightarrow \infty) \end{aligned}$$

In a similar vein, one can prove that if $\alpha(T)$ is any differentiable function with $\alpha'(T) < 0$ and a (unique) root $T_0 > 0$, then the solution to (A.1) converges to the Dirac measure δ_{T-T_0} in the sense of weak convergence of measures.

Appendix B. Formal steady state of Eqs. (3.9)–(3.11)

We now analyze a (formal) steady state of the system of Eqs. (3.9)–(3.11). This discussion can be made more rigorous using a suitable weak formulation, but we constrain ourselves to a formal approach. This formal steady state is the quadruple $(\bar{c}_1^u, \bar{c}_2^u, \bar{T}_1, \bar{T}_8)$ such that $c_1(t, \mathbf{x}) = \bar{c}_1^u$, $c_2(t, \mathbf{x}) = \bar{c}_2^u$, $R(t, \mathbf{x}, T_1, T_8) = \delta(T_1 - \bar{T}_1) \times \delta(T_8 - \bar{T}_8)$ is a solution, where again δ denote Dirac delta distributions. The corresponding equations are

$$\tilde{\gamma}(\bar{c}_1^u, \bar{c}_8^u, \bar{T}_1) = 0, \quad \tilde{\delta}(\bar{c}_8^u, \bar{T}_8) = 0, \quad \tilde{\nu} \frac{\bar{c}_8^u}{\bar{c}_8^u + 1} \bar{T}_8 - \bar{c}_1^u = 0,$$

$$\tilde{\mu} \frac{\bar{c}_1^u}{\bar{c}_1^u + f\bar{c}_8^u + 1} \bar{T}_8 - \tilde{\pi}_8 \bar{c}_8^u = 0.$$

This yields the following values:

$$\bar{c}_1^u = \tilde{\mu}\tilde{\nu} \frac{\tilde{c}_1\tilde{\gamma}_2}{2\tilde{\mu}\tilde{\nu} - \tilde{\gamma}_2\tilde{\delta}_2\tilde{\pi}_8} \tag{B.1}$$

$$\bar{c}_8^u = \frac{\tilde{c}_1\tilde{\delta}_2}{\tilde{\nu}} \tag{B.2}$$

$$\bar{T}_8 = \frac{1 + \bar{c}_8^u}{\tilde{\delta}_2} \tag{B.3}$$

$$\bar{T}_1 = \frac{\delta_2 \bar{\kappa}_8 (1 + \bar{c}_1^u + f \bar{c}_8^u)}{\bar{\nu} \bar{\mu}} \quad (\text{B.4})$$

A positive steady state exists if $\bar{c}_1^u > 0$.

Appendix C. Supplementary data

Supplementary data associated with this paper can be found in the online version at <http://dx.doi.org/10.1016/j.jtbi.2013.12.004>.

References

- Alber, Mark, Chen, Nan, Glimm, Tilmann, Lushnikov, Pavel M., 2006. Multiscale dynamics of biological cells with chemotactic interactions: from a discrete stochastic model to a continuous description. *Phys. Rev. E* 73 (5) 051901.
- Alber, M., Chen, N., Lushnikov, P., and S. Newman 2007. Continuous macroscopic limit of a discrete stochastic model for interaction of living cells, *Phys. Rev. Lett.* 99, 168102.
- Alber, M., Hentschel, H.G.E., Kazmierczak, B., Newman, S.A., 2005. Existence of solutions to a new model of biological pattern formation. *J. Math. Anal. Appl.* 308 (1), 175–194, <http://dx.doi.org/10.1016/j.jmaa.2004.11.026>, ISSN 0022-247X.
- Alber, M., Glimm, T., Hentschel, H.G.E., Kazmierczak, B., Zhang, Y.-T., Zhu, J., Newman, S.A., 2008. The morphostatic limit for a model of skeletal pattern formation in the vertebrate limb. *Bull. Math. Biol.* 70 (2), 460–483, ISSN 0092-8240.
- Anguige, K., Schmeiser, C., 2009. A one-dimensional model of cell diffusion and aggregation, incorporating volume filling and cell-to-cell adhesion. *J. Math. Biol.* 58 (3), 395–427, <http://dx.doi.org/10.1007/s00285-008-0197-8>, ISSN 0303-6812.
- Armstrong, N.J., Painter, K.J., Sherratt, J.A., 2006. A continuum approach to modelling cell–cell adhesion. *J. Theor. Biol.* 243 (1), 98–113, <http://dx.doi.org/10.1016/j.jtbi.2006.05.030>, ISSN 0022-5193.
- Bhat, R., Lerea, K.M., Peng, H., Kaltner, H., Gabius, H.J., Newman, S.A., 2011. A regulatory network of two galectins mediates the earliest steps of avian limb skeletal morphogenesis. *BMC Dev. Biol.* 11, 6.
- Billingsley, P., 1999. *Convergence of Probability Measures*, Wiley Series in Probability and Statistics: Probability and Statistics, second edition John Wiley & Sons, Inc., New York <http://dx.doi.org/10.1002/9780470316962>, ISBN 0-471-19745-9, A Wiley-Interscience Publication.
- Christley, S., Alber, M.S., Newman, S.A., 2007. Patterns of mesenchymal condensation in a multiscale, discrete stochastic model. *PLoS Comput. Biol.* 3 (April (4)), e76.
- Diekmann, O., 1999. Modeling and analysing physiologically structured populations. In: *Mathematics inspired by biology* (Martina Franca, 1997), Lecture Notes in Mathematics, vol. 1714, Springer, Berlin, pp. 1–37. URL <http://dx.doi.org/10.1007/BFb0092374>.
- Downie, S.A., Newman, S.A., 1994. Morphogenetic differences between fore and hind limb precartilaginous mesenchyme: relation to mechanisms of skeletal pattern formation. *Dev. Biol.* 162 (March (1)), 195–208.
- Downie, S.A., Newman, S.A., 1995. Different roles for fibronectin in the generation of fore and hind limb precartilaginous condensations. *Dev. Biol.* 172 (December (2)), 519–530.
- Forgacs, G., Newman, S.A., 2005. *Biological Physics of the Developing Embryo*. Cambridge University Press.
- Frenz, D.A., Akiyama, S.K., Paulsen, D.F., Newman, S.A., 1989a. Latex beads as probes of cell surface–extracellular matrix interactions during chondrogenesis: evidence for a role for amino-terminal heparin-binding domain of fibronectin. *Dev. Biol.* 136 (November (1)), 87–96.
- Frenz, D.A., Jaikaria, N.S., Newman, S.A., 1989b. The mechanism of precartilaginous mesenchymal condensation: a major role for interaction of the cell surface with the amino-terminal heparin-binding domain of fibronectin. *Dev. Biol.* 136 (November (1)), 97–103.
- Gabius, H., 2009. *The Sugar Code*. Wiley, ISBN 9783527320899, URL (http://books.google.com/books?id=wST5C_JM91AC).
- Gierer, A., Meinhardt, H., 1972. A theory of biological pattern formation. *Kybernetik* 12 (December (1)), 30–39.
- Glazier, J.A., Graner, F., 1993. Simulation of the differential adhesion driven rearrangement of biological cells. *Phys. Rev. E Stat. Phys. Plasmas Fluids Relat. Interdiscip. Top.* 47 (March (3)), 2128–2154.
- Glimm, T., Headon, D., Kiskowski, M.A., 2012. Computational and mathematical models of chondrogenesis in vertebrate limbs. *Birth Defects Res. C Embryo Today* 96 (June (2)), 176–192.
- Hall, B.K., Miyake, T., 2000. All for one and one for all: condensations and the initiation of skeletal development. *Bioessays* 22 (February (2)), 138–147.
- Hentschel, H.G.E., Glimm, T., Glazier, J.A., Newman, S.A., 2004. Dynamical mechanisms for skeletal pattern formation in the vertebrate limb. *Proc. R. Soc. Lond. B Biol. Sci.* 271 (August (1549)), 1713–1722.
- Kiskowski, M.A., Alber, M.S., Thomas, G.L., Glazier, J.A., Bronstein, N.B., Pu, J., Newman, S.A., 2004. Interplay between activator–inhibitor coupling and cell–matrix adhesion in a cellular automaton model for chondrogenic patterning. *Dev. Biol.* 271 (July), 372–387.
- Lorda-Diez, C.I., Montero, J.A., Diaz-Mendoza, M.J., Garcia-Porrero, J.A., Hurlle, J.M., 2011. Defining the earliest transcriptional steps of chondrogenic progenitor specification during the formation of the digits in the embryonic limb. *PLoS One* 6 (9), e24546.
- Meinhardt, H., Gierer, A., 2000. Pattern formation by local self-activation and lateral inhibition. *Bioessays* 22 (August (8)), 753–760.
- Miura, T., Shiota, K., Morriss-Kay, G., Maini, P.K., 2006. Mixed-mode pattern in Doublefoot mutant mouse limb–Turing reaction–diffusion model on a growing domain during limb development. *J. Theor. Biol.* 240 (June (4)), 562–573.
- Müller, G.B., 2007. Evo-devo: extending the evolutionary synthesis. *Nat. Rev. Genet.* 8 (December (12)), 943–949.
- Newman, S.A., Bhat, R., 2007. Activator–inhibitor dynamics of vertebrate limb pattern formation. *Birth Defects Res. C Embryo Today* 81 (December (4)), 305–319.
- Newman, S.A., Bhat, R., 2008. Dynamical patterning modules: physico-genetic determinants of morphological development and evolution. *Phys. Biol.* 5 (1), 015008.
- Newman, S.A., Frisch, H.L., 1979. Dynamics of skeletal pattern formation in developing chick limb. *Science* 205 (August (4407)), 662–668.
- Newman, S.A., Christley, S., Glimm, T., Hentschel, H.G., Kazmierczak, B., Zhang, Y.T., Zhu, J., Alber, M., 2008. Multiscale models for vertebrate limb development. *Curr. Top. Dev. Biol.* 81, 311–340.
- Ros, M.A., Lyons, G.E., Mackem, S., Fallon, J.F., 1994. Recombinant limbs as a model to study homeobox gene regulation during limb development. *Dev. Biol.* 166 (November (1)), 59–72.
- Salazar-Ciudad, I., Jernvall, J., 2010. A computational model of teeth and the developmental origins of morphological variation. *Nature* 464 (March (7288)), 583–586.
- Salazar-Ciudad, I., Jernvall, J., Newman, S.A., 2003. Mechanisms of pattern formation in development and evolution. *Development* 130 (May), 2027–2037.
- Saunders, J.W., 1948. The proximo–distal sequence of origin of the parts of the chick wing and the role of the ectoderm. *J. Exp. Zool.* 108 (August (3)), 363–403.
- Sheth, R., Marcon, L., Bastida, M.F., Junco, M., Quintana, L., Dahn, R., Kmita, M., Sharpe, J., Ros, M.A., 2012. Hox genes regulate digit patterning by controlling the wavelength of a Turing-type mechanism. *Science* 338 (December (6113)), 1476–1480.
- Thieme, H.R., 2003. *Mathematics in Population Biology*. Princeton Series in Theoretical and Computational Biology. Princeton University Press, Princeton, NJ, ISBN 0-691-09290-7; 0-691-09291-5.
- Turing, A.M., 1952. The chemical basis of morphogenesis. *Bull. Math. Biol.* 52 (1–2), 153–197.
- Wolpert, L., 1969. Positional information and the spatial pattern of cellular differentiation. *J. Theor. Biol.* 25 (October (1)), 1–47.
- Wolpert, L., 1989. Positional information revisited. *Development* 107 (Suppl.), 3–12.
- Zhang, Y.T., Alber, M.S., Newman, S.A., 2013. Mathematical modeling of vertebrate limb development. *Math. Biosci.* 243 (May (1)), 1–17.
- Zhu, J., Zhang, Y.T., Alber, M.S., Newman, S.A., 2010. Bare bones pattern formation: a core regulatory network in varying geometries reproduces major features of vertebrate limb development and evolution. *PLoS One* 5 (5), e10892.
- Zwilling, E., 1964. Development of fragmented and dissociated limb bud mesoderm. *Dev. Biol.* 89 (February), 20–37.